Wiley
Indoor Air
Volume 2024, Article ID 9593123, 21 pages
https://doi.org/10.1155/2024/9593123

WILEY

*Research Article*

# How Does the Interaction of the Human Thermal Plume and Breathing Affect the Microenvironment and Macroenvironment of an Elevator Cabin?

**Farzad Pourfattah**,[1] **Weiwei Deng**,[1] **and Lian-Ping Wang**[1,2]

[1]*Guangdong Provincial Key Laboratory of Turbulence Research and Applications, Center for Complex Flows and Soft Matter Research and Department of Mechanics and Aerospace Engineering, Southern University of Science and Technology, Shenzhen 518055, China*
[2]*Guangdong-Hong Kong-Macao Joint Laboratory for Data-Driven Fluid Mechanics and Engineering Applications, Southern University of Science and Technology, Shenzhen 518055, China*

Correspondence should be addressed to Lian-Ping Wang; wanglp@sustech.edu.cn

Received 9 August 2023; Revised 16 February 2024; Accepted 29 April 2024; Published 22 May 2024

Academic Editor: Xiaohu Yang



The details of the interaction of human thermal plume and breathing activities are simulated in the current study of an unsteady turbulent flow field in an elevator cabin. Air velocity and temperature distributions of the circulation flow pattern (i.e., the macroenvironment), the breathing-scale microenvironment's characteristics, and the thermal plume's fate are analyzed. The current study is aimed at showing how respiratory activities such as breathing and human thermal plumes affect the flow field and respiratory contaminants dispersion pattern in a nonventilated enclosed environment (the elevator cabin). The results from three cases, i.e., breathing thermal manikins, nonbreathing thermal manikins, and isothermal breathing manikins, are contrasted to unveil better the effects of human thermal plume and breathing on the flow field, including the velocity distribution, dispersion pattern of the exhaled contaminant, the human body's heat transfer coefficient, and the large-scale flow pattern. Results reveal that breathing inhalation increases the upward velocity of the thermal plume on the one hand, which directly affects the microenvironment and indirectly impacts the macroenvironment due to the more vigorous reflected thermal plume. On the other hand, the upward thermal plume reduces the penetration length of the exhaled jet. Breathing activities create ring vortices that connect the microenvironment and the macroenvironment. The circulation flow features a downward flow in the cabin's center, affecting the vortex strength and contaminant dispersion pattern. Overall, the human thermal plume and human breathing make comparable contributions to the resulting elevator-cabin flow characteristics.

## 1. Introduction

Inhaled air quality impacts people's health in buildings. Indoor air quality is critical to providing a comfortable environment. Keeping the indoor environment fresh and safe and minimizing contaminants are essential through ventilation. A more significant role will be played by the indoor flow pattern if the source of the contamination is inside (e.g., smoking or released aerosols from respiratory activities). Therefore, it is crucial to understand the characteristics of the flow field in the indoor environment to properly design a ventilation system to control the dispersion of any indoor source of contaminant.

During 2020-2022, the world has been affected by the epidemic caused by the COVID-19 virus. The ongoing COVID-19 pandemic has highlighted that one of the main transmission routes of SARS-CoV-2 is the airborne transmission of infectious respiratory droplets between indoor occupants [1]. Hence, minimizing internal contaminant dispersion has received attention from many governments and researchers. It appears that the current epidemic may affect air conditioning standards from being "comfort-based" to

"health-based." Currently, indoor airflow guidelines do not prioritize preventing virus/aerosol transmission. Fluid mechanics and heat transfer communities can play a pioneering role in formulating updated standards by conducting proper investigations into indoor flow patterns.

The flow pattern created by the air conditioning system determines the severity of the pollutant or virus aerosol dispersion. The effects of ventilation system arrangement on airflow pattern and indoor air quality have been widely investigated by experimental [2] and numerical [3] methods.

Conducting the experimental study on the air conditioning arrangements for different environments is difficult, expensive, and time-consuming. Numerical simulations can be a good alternative, although the indoor flow behavior is complex from the fluid mechanics point of view. The indoor flows feature jet impingement (inlets of the ventilation systems), flow separation, circulation, reattachment, and vortices [4]. Numerical simulation of the indoor environment is further complicated when the actual condition of human presence is considered. The schematic of the local flow pattern around a human model is shown in Figure 1. As a result of breathing, coughing, and sneezing, and the temperature difference between body and indoor environment, the presence of humans in an indoor environment contributes to local flow features.

In indoor flow investigations, the characteristics of the human thermal plume, such as the velocity magnitude and direction, are important because they can carry suspended contaminants into the microenvironment. Lewis et al. [5] referred to flow fields near of the human body as microenvironments. The thickness of the microenvironment is affected by the temperature difference between the human body surface and the adjacent air, the type of clothing, body geometry, ventilation, human respiratory flows, and even furniture arrangement in a closed space [6]. Also, several factors influence air quality in the microenvironment, including the ventilation systems, ambient airflow, the body's local thermal plumes, and the location of pollution sources [6]. The experimental data in the literature indicates that the maximum speed of thermal plumes of human manikins while standing and sitting is 0.24 m/s [7] and 0.15 m/s [8], respectively, which can affect the air distribution in a closed space [9] and the distribution of any contaminant [10]. The human thermal plume can influence the contaminant concentration in the microenvironment; as Salmanzadeh et al. [11] showed, it was approximately twice as high in the respiratory area of heated manikins as it was in unheated manikins (isothermal manikins).

Additionally, the effect of the thermal plume on contaminant intake by the respiratory system depends on the location of the pollution source [12]. If the height of the contaminant source is lower than the respiratory system, the bouncy flow can facilitate entering contaminant into the respiratory system [13]. For example, suspended aerosols ranging from 0.3 to 1.3 $\mu$m in diameter can be carried by the thermal plume and absorbed into the lower respiratory tract, increasing the risk of infection [13]. On the other hand, if the height of the contaminant is as high as the human body, forming of a vertical upward thermal plume can prevent airborne particles from entering the respiratory tract (if there is no circulation). Based on the numerical results of Feng et al. [13], when the thermal plume of a human is thick and faster, it is more difficult for nasal aerosols to penetrate the plume. It can be concluded that the thermal plume can be a double-edged sword. Therefore, the human thermal plume could significantly affect airborne particle/virus aerosol dispersion in the indoor environment. The flow field characteristics around the human body have been widely investigated [6, 12, 14], and the effect of the thermal plume on inhalation exposure to particulate matter is discussed in the recent review paper of Zong et al. [15].

The flow pattern around the human body can be affected by the ventilation system arrangement, air temperature, and body posture/temperature [16]. In addition to the thermal plume, as shown in Figure 1, the interaction of human respiratory activities with the ambient air, creating a ring vortex that complicates the flow field. Although the maximum velocity of coughing and sneezing is greater than the velocity of normal breathing, in any human respiratory activity, the ring vortex has been observed [17, 18]. The strength of the ring vortex is important because it is close to the breathing zone (or the microenvironment) and can facilitate pollution penetration from the macroenvironment to the microenvironment and increases the number of inhaled contaminants.

Tracking the dispersion pattern of contaminants such as virus aerosol, chemical species, and bacteria is one of the critical requirements in designing a health-based ventilation system. In the literature, tracking the contaminants released by human respiratory activities has been conducted by tracer gas [19] or particle [20]. Investigations that used tracer gas assumed the size of released particles by respiratory activities was in the micron-size range, and the Stokes number is much less than 1; therefore, the microparticles follow the flow field closely [10].

Modelling the released exhaled jet as tracer gas such as $N_2O$ [21] and $CO_2$ [19] is a common method in the literature, which is also utilized in the current modeling. Previous investigations showed that the breathing inertia force of the exhaled air (tracer gas) could influence the buoyancy force and thermal plume in the breathing zone [19]. The exhaled air through the mouth can penetrate the boundary layer of the human thermal plume [4]. On the other hand, based on the experiment results of Cheng et al. [22], breathing through the nose had much more impact on thermal plumes around the manikin than breathing through the mouth. Bjørn and Nielsen [4] showed that exhalation of air through the nose and mouth substantially influences the personal exposure level. Therefore, the interaction of the thermal plume and breathing is critical in determining the airborne transmission in the short range (significantly less than 0.5 m) [23].

Due to the recent epidemic, many investigations have been conducted concerning the dispersion pattern of the airborne pathogen/virus aerosol in different indoor environments [24–28] such as classrooms [29, 30], offices and terminals [31], cabin of airplanes [32], buses [33, 34], trains [35], dental clinics [36], and elevator cabins [37–39]. Details of the conducted investigations on the characteristics of the

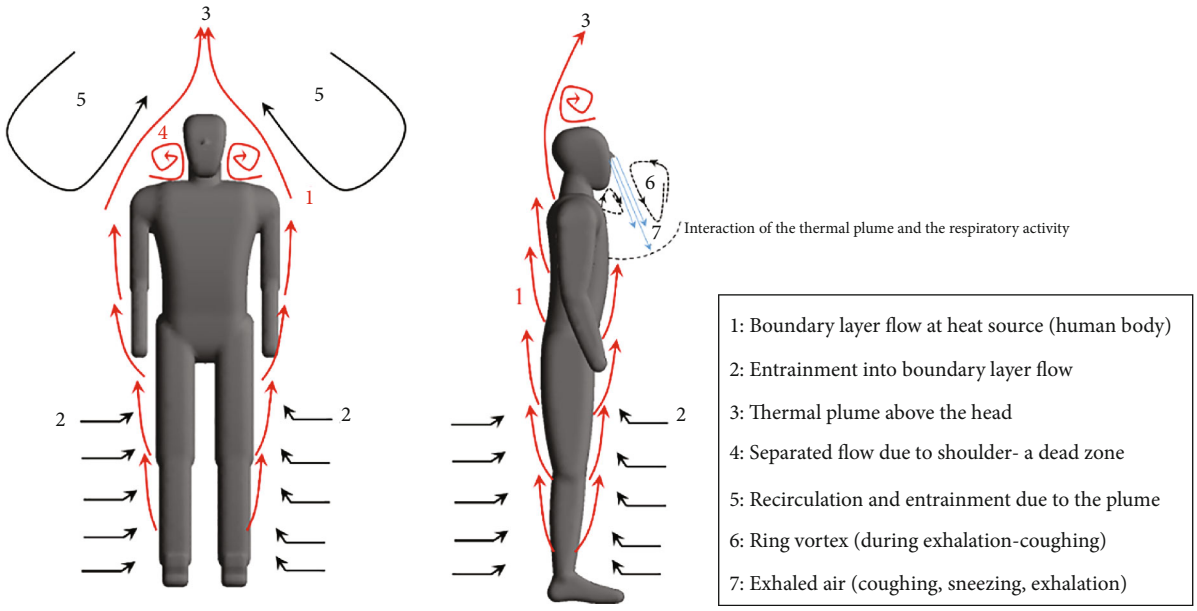


Figure 1: Schematic of flow pattern in an indoor environment around a human model.

flow field and particle dispersion pattern in an elevator cabin are presented in Table 1. Based on Table 1, most of the investigations tracked the released particles in the indoor environment without modeling the human thermal plume of a real human model. Numerous studies examined the thermal plume of a manikin in the middle of the room but did not determine its fate. However, it may be reflected by the ceiling and cause circulation and vertical flow in the macroenvironment. Meanwhile, the interaction of the formed thermal plumes of humans that stand side by side can also contribute to the microenvironment flow. Furthermore, if a human stands near the indoor environment wall, the thermal plume velocity will be accelerated. This is different from a human standing in the middle of the room. Therefore, simultaneous considerations of breathing, thermal plumes, and domain boundaries are necessary to understand contaminant transport.

Based on the conducted literature review mentioned above, the effect of the interaction of the human thermal plume and breathing activity on the contaminant dispersion which is released by human breathing in a closed environment at a real scale of an elevator cabin has not been adequately addressed. For discovering that point, this study explores the above multiscale and multiphysics interaction by considering the situation in an elevator cabin where six thermal breathing manikins are present. The effects of the thermal plume, breathing through the nose, and the interactions of the thermal plume with breathing and cabin walls are examined systematically.

The remainder of the paper is organized as follows. Section 2 provides the problem statement and the model setup, followed by a description of the simulation method in Section 3. Simulation results are discussed in details in Section 4, including interactions of the human thermal plumes and breathing during both exhalation and inhalation, unsteady local flow features, large-scale flow patterns, thermal transport, and integral measures of the thermal plumes. Finally, conclusions are summarized in Section 5.

## 2. Problem Statement

This section presents details of the computational domain, specifications of the thermal human model, and the adopted boundary conditions.

*2.1. Computational Domain and Human Model.* In this investigation, the multiscale flows in an elevator cabin occupied by six breathing thermal manikins are simulated to investigate the flow patterns at both the nose scale and the cabin scale and the contaminant dispersion (tracer gas distribution) due to human breathing. The cabin's dimensions are $2\,\mathrm{m}\,(\mathrm{width}) \times 2\,\mathrm{m}\,(\mathrm{depth}) \times 2.5\,\mathrm{m}\,(\mathrm{height})$, a standard cabin used in commercial and residential buildings. Six thermal manikins are present in the cabin. In the literature, many arrangements of thermal manikins were investigated. To capture more details of the airflow characteristics in the microenvironment, the geometry of the human model is crucial because the human geometry can affect the human thermal plume's characteristics. It is clear that using more realistic manikins increases accuracy and the computational cost [12].

A literature survey was done to select the human model [44–46]. Based on the literature, although the details of the human model can influence the microenvironment characteristics, the gap between the legs is mentioned as the most crucial geometrical feature that affects the thermal plume pattern because the upward flow (thermal plume) is divided into two parts due to the gap. Due to the details and availability of the model, the human model used by Kilic and Sevilgen [44] and Ahmed et al. [45] was selected as a thermal manikin in the current study. The schematic of the computational domain is presented in Figure 2. As seen, three

Table 1: Details of the recent CFD-based investigations on the flow dynamics and particle tracking method in an elevator cabin.

| Ref. | Human thermal plume | Real human geometry | Time depended respiratory activity | Particle/droplet/gas tracer |
|---|---|---|---|---|
| [37] | ✓ | × | ✓ | Particle |
| [39] | × | × | ✓ | Droplet |
| [40] | × | × | ✓ | Particle |
| [41] | ✓ | × | × | × |
| [42] | × | × | ✓ | Droplet |
| [43] | ✓ | × | ✓ | Particle |

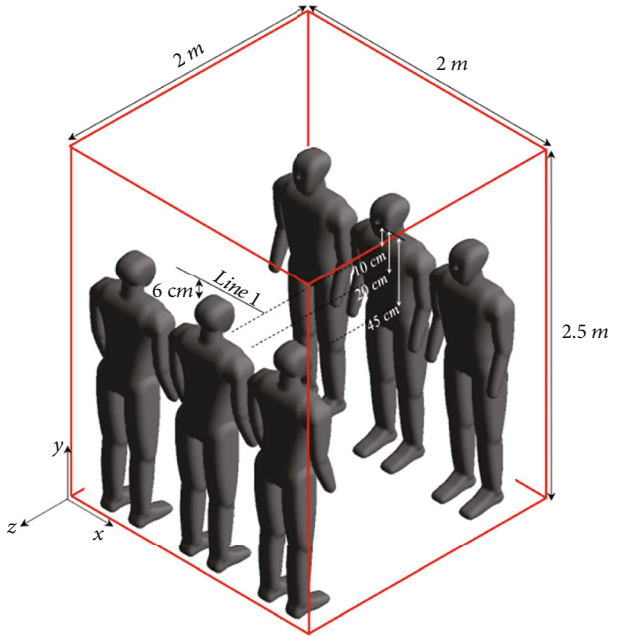


Figure 2: Computational domain and thermal manikins in the current simulation.

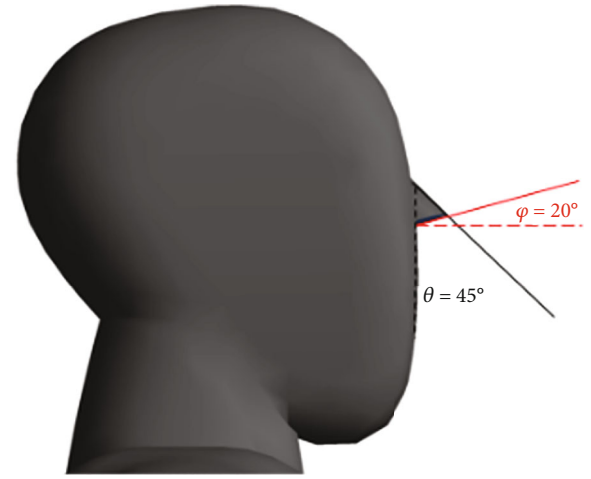


Figure 3: Nose shape of the human manikin in the current simulation: surface area: 0.056 $cm^2$, front angle $\varphi$: 20°, and side angle $\theta$: 45.

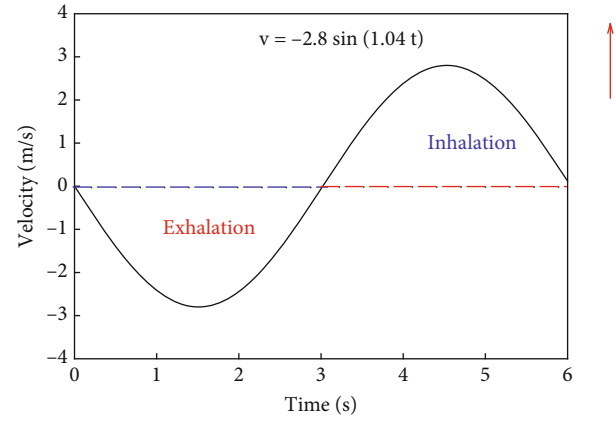


Figure 4: The applied velocity boundary condition for breathing [52].

manikins stand side by side on the left and right sides of the elevator cabin.

In the current problem, breathing through the nose is simulated. The nostril's geometry can significantly affect the microenvironment because the exhaled air-jet characteristics, such as mass flow rate and penetration angle, depend on the nostril's geometrical characteristics. A literature survey showed that different geometries were considered as the breathing system. Some investigations considered two angles for the nostril, including the side and the normal angle. The side angle ranges from 35 to 45 degrees [13, 22, 47], and the surface area ranges between 0.56 and 0.63 $cm^2$ [19]. Figure 3 shows the schematic of the modeled nostril shape in the current simulation. The side and front angles are assumed to be 45 and 20 degrees, respectively. The cross-section area is 0.056 $cm^2$.

### 2.2. Boundary Conditions

*2.2.1. Breathing.* Boundary conditions associated with unsteady respiratory activities can significantly influence the exhaled air jet characteristics. The flow rate, flow direction, and area of the released jet depend on the type of respiratory activity, sexual and physical characteristics and body conditions (at rest, usual activities, light exercise, or heavy sports). Although the so-called normal condition of humans was considered in the literature, experimental investigations have presented different velocity profiles for the normal conditions that are not consistent, and the reported velocity varies significantly (for example, 16–50 m/s has been reported for coughing) [48].

All respiratory activities are unsteady; whereas, in some numerical simulations, a constant velocity profile has been applied for breathing and coughing [49]. Numerical

Table 2: Literature survey on the applied boundary condition on the human body.

| The applied boundary condition | References |
|---|---|
| Constant temperature | 34°C [6]; 26.6°C [9]; 31°C–33.7°C [12]; head, arm, upper, and lower: 33, 24, 27, and 28°C [13]; 34°C [19]; 33–34°C [22]; 31°C [60]; 31°C [61]; with and without clothes: 26.6°C and 32.2°C [53]; head, neck, chest, waist, thighs, and calves: 30.8, 32.5, 32.4, 34.2, 34.1, and 27°C [56]; heat and other parts: 32°C and 30°C [62]; 34°C [63] |
| Constant heat flux | 94 W [64], 100 W/m$^2$ [44], head and neck: 150 W/m$^2$, other parts of the body: 50 W/m$^2$ [10, 65] |

Table 3: The applied boundary condition in the current simulation.

| Boundary | Applied boundary condition |
|---|---|
| Human body | No slip wall; constant temperature; head, arm, upper, and lower are 33, 24, 27, and 28°C, respectively [13] |
| Exhaled air through nose | Transient sinusoidal velocity profile, air with 0.04 $N_2O$ [55], temperature: 35°C [13] |
| Cabin's wall | No slip wall; constant temperature: 24°C [13] |

investigations considering more realistic boundary conditions utilized a time-dependent velocity profile for breathing and coughing [50]. The breathing velocity profile includes two phases, inhalation and exhalation phases. During inhalation, the air is inhaled through the nose and causes an upward flow, whereas exhalation releases the air jet into the microenvironment as a downward flow. The breathing process has different characteristics in the literature, including the breathing period (number of breaths per minute) and maximum velocities associated with breathing profiles [51]. More details of the breathing, coughing, and sneezing velocity profiles in the literature were presented in the review paper by Pourfattah et al. [48].

Figure 4 illustrates the adopted velocity boundary condition [52] for breathing. As seen in Figure 4, one breathing cycle occurs in 6 seconds, and the velocity magnitude peaks at 2.8 m/s [52], and four breathing cycles have been modeled in the current simulation. The turbulent intensity of the exhaled jet is considered to be 0.1% [53].

Also, the thermal boundary condition of the exhaled air affects the density of the ejected air and the buoyancy force. The mean temperature of the exhaled air is influenced by the inhaled temperature (i.e., ambient) [54]. Based on the literature [13, 54], at an ambient temperature of 20°C, the mean temperature of the exhaled air is approximately 34-35°C. In addition, the exhaled air differs from the ambient air or water vapor. In the current simulation, the exhaled air is assumed to be at 35°C and the exhaled particles are modeled by a tracer gas. Literature review revealed that different volume fraction/mass fraction $N_2O$ or $CO_2$ has been applied on the mouth or nose to study the dispersion/diffusion pattern of the exhaled air [54, 55]. In this simulation, "$N_2O$" is used as tracer gas, with a $N_2O$ mass fraction of 0.04 at the nose [55] to track the dispersion of the exhaled particle/contaminant/virus. It is worth mentioning that the amount of the inhaled contaminant depends on the inhaled air velocity and contaminant volume fraction in the breathing zone.

*2.2.2. Human Body Surface Temperature.* As mentioned before, the temperature difference between the body and the environment causes the buoyancy force, which drives the thermal plume formation at the body-size scale. Therefore, the type of the applied thermal boundary condition on the human body surface can play a significant role in the dynamic characteristics of the thermal plume. Based on the literature review, the experimental studies applied constant heat flux to the human body surface. When the thermal conditions became stabilized, the data was recorded and analyzed [56]. In the numerical simulation, two options exist to treat the thermal boundary condition on the body surface, including the constant temperature or the heat flux. In the simulation of the flow field and heat transfer in the indoor environment, choosing the wall boundary condition type depends on the modeling the radiation heat transfer. Suppose the wall temperature of the indoor environment and body surface are considered constant, there is no need to model the radiation heat transfer because the consistent applied temperatures on the human body and walls indicate that there is a thermal balance between walls [9, 11, 57], whereas modeling radiation will be needed if the constant heat flux is applied to walls to capture the walls temperature variations over time [58, 59].

It is clear that the head of a human is warmer than other parts of the body. In some simulation, the amount of the applied heat flux or the value of the temperature on the head is greater than other parts. However, the same heat flux or temperature has been applied to all parts of the body [60, 61]. A brief literature survey on the applied boundary conditions on the human body is presented in Table 2. The human body surface temperature and the used heat flux range from 30 to 37°C and 75 to 100 W/m$^2$, respectively. In the current simulation, due to the large number of nodes in the computational grid (about 17 million nods after adaption), to reduce the computational time and cost, constant wall temperatures are applied to the different parts of the body surface and the radiation heat transfer is not modeled. Based on Table 2, Feng et al. [13] applied more realistic boundary conditions on the human body surface that assumed the head and arms are exposed to the environment while the other body sections are covered by clothing. They divided the human body into head, arms, upper body, and lower body and applied the constant temperature to each section. The same treatment is used in the current modeling.

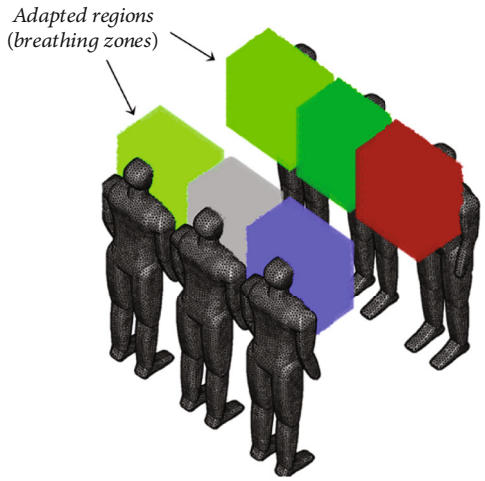


Figure 5: Grid-refinement regions in the computational domain.

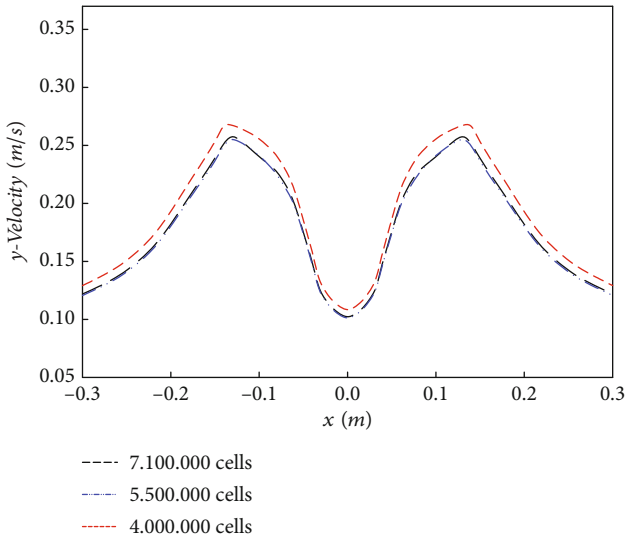


Figure 6: Velocity profile on a horizontal line 6 cm above the head.

This section is concluded by Table 3 which lists all the applied boundary conditions in the current study.

## 3. Numerical Method and Setup

*3.1. Governing Equations.* Respiratory activities such as breathing can emit droplets, aerosol particles, and viruses into the environment. Based on the literature, the generated droplets/particles from breathing are mainly under 1 $\mu$m in size, as determined by Papineni and Rosenthal [66]. It should be mentioned that medium-sized droplets that ejected by respiratory activities evaporate immediately, and the large droplets settle down on the ground [67]. Since the Stokes number of the released particles by breathing (under 1 $\mu$m) is less than 1, such tiny submicron droplets and dried-out nuclei residues follow the flow closely. As a result, tracer gas was considered an effective method for mimicking pathogen-laden aerosol droplet dispersion. The species transport model has been widely used to track aerosol dispersions [4, 68] and is implemented in the current simulation.

Table 4: Validation of the current numerical results.

| Current result | Maximum velocity of the thermal plume | Difference (%) |
|---|---|---|
| 0.25 m/s | 0.235 m/s [62] | 6% |
| | 0.24 m/s [9] | 4% |
| | 0.225 m/s [8] | 11% |

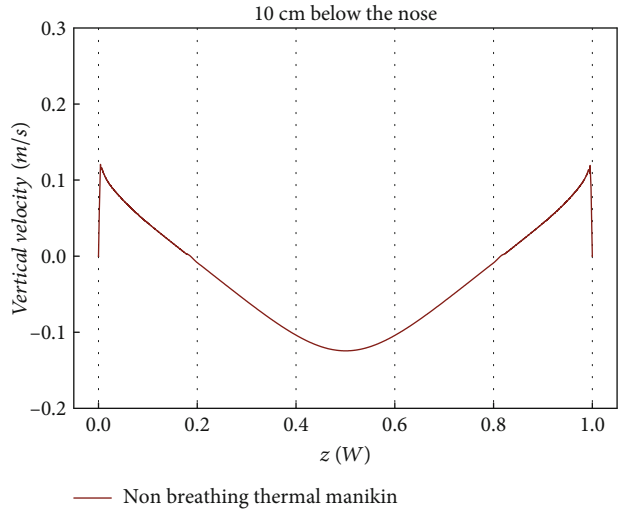


Figure 7: Velocity profile in the middle of the cabin, thermal manikin without breathing, 10 cm below the nose.

The flow field and heat transfer in the elevator cabin are simulated by the finite volume method (ANSYS-Fluent 19.2). The flow field is modeled by the three-dimensional and unsteady Reynolds-averaged Navier-Stokes (RANS) equations, combined with continuity and energy equations. The maximum number of iterations to be performed per time step (0.001 s) was considered 25. The SIMPLEC algorithm was utilized with a second-order discretization scheme for the convective terms. The governing equations are as follows:

Continuity equation:

$$\frac{\partial \rho}{\partial t} + \nabla . \left( \rho \vec{V} \right) = 0. \tag{1}$$

Momentum equation:

$$\frac{\partial}{\partial t} \left( \rho \vec{V} \right) + \nabla . \left( \rho \vec{V} . \vec{V} \right) = -\nabla P + (\mu + \mu_t) \nabla^2 V + (\rho_0 - \rho) g. \tag{2}$$

It should be noted that the last term on the right-hand side is the buoyancy force term, and it is computed by the ideal gas law for an incompressible flow.

$$\rho = \frac{P}{(R/M_w)T}, \tag{3}$$

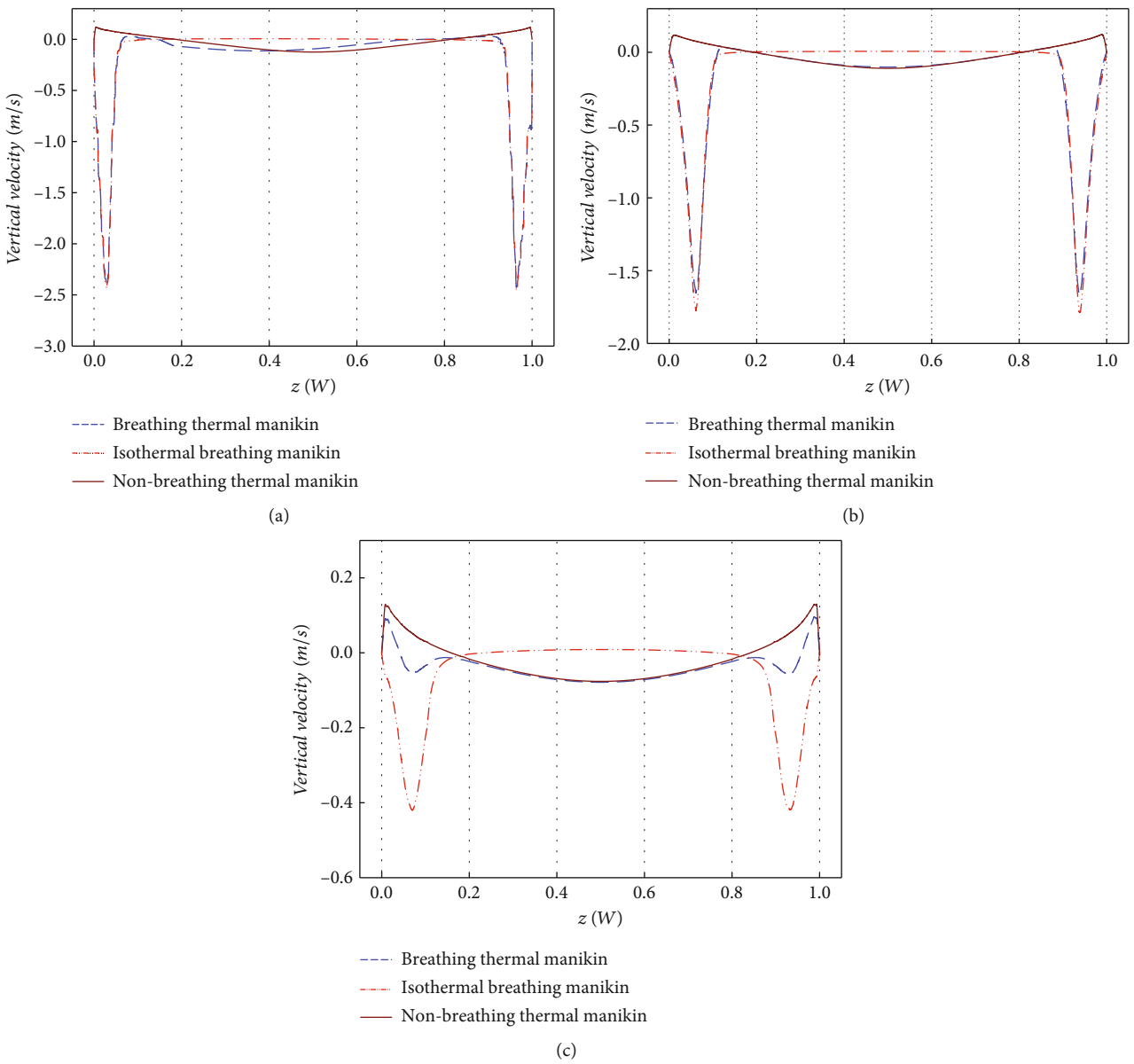


FIGURE 8: Velocity profile in the middle of the cabin at different distance of the nose, during exhalation. (a) 10 cm below the nose. (b) 20 cm below the nose. (c) 45 cm below the nose.

where $P$, $R$, and $M_w$ are the operating pressure, the universal gas constant, and molecular weight of the gas, respectively.

Energy equation:

$$\frac{\partial}{\partial t}(\rho E)+\nabla.\left(\vec{V}(\rho E+P)\right)=\nabla.\left(\rho(k+k_t)\nabla T-\sum h_j\overrightarrow{J_j}+\left(\overline{\overline{\tau}}.\vec{V}\right)\right), \tag{4}$$

where $E$ (total energy) is expressed as

$$E=\sum Y_j h_j-\frac{P}{\rho}+\frac{V^2}{2}, \tag{5}$$

where $\rho$ is the density, $\vec{V}$ represents the components of mean airflow velocity in the Cartesian coordinate, $P$ is the pressure, $\mu$ and $\mu_t$ are dynamic molecular and turbulent (eddy) viscosities, respectively, $g$ is the gravitational acceleration, and $k$ and $k_t$ are the molecular conductivity and turbulent conductivity, respectively. $h_j$ is the enthalpy of species, $\overrightarrow{J_j}$ is the diffusion flux of species, and $\overline{\overline{\tau}}$ is the stress tensor.

The eddy viscosity $(\mu_t)$ is evaluated by utilizing a turbulence model. Comprehensive surveys have compared the results of different turbulence modeling strategies for indoor flows [69]. The majority of RANS simulations emphasized that k-ε RNG accuracy is more acceptable than other RANS

models in the simulation of the indoor flow [29, 32]. Therefore, in the current simulation, k-$\varepsilon$ RNG is utilized. The transport equations for the k-$\varepsilon$ RNG model are as follows:

$$\begin{aligned}
\mu_t &= \frac{\rho c_\mu k^2}{\varepsilon} c_\mu = 0.0845,\\
u_j \frac{\partial k}{\partial x_j} &= \tau_{ij} \frac{\partial u_i}{\partial x_j} - \varepsilon + \frac{\partial}{\partial x_j}\left[(\alpha_k \upsilon_{\text{eff}}) \frac{\partial k}{\partial x_j}\right],\\
u_j \frac{\partial \varepsilon}{\partial x_j} &= C_{\varepsilon 1} \frac{\varepsilon}{k} \tau_{ij} \frac{\partial u_i}{\partial x_j} - C_{\varepsilon 2} \frac{\varepsilon^2}{k} + \frac{\partial}{\partial x_j}\left[(\alpha_\epsilon \upsilon_{\text{eff}}) \frac{\partial \varepsilon}{\partial x_j}\right] - R_\varepsilon,\\
C_{\varepsilon 1} &= 1.42,\\
C_{\varepsilon 2} &= 1.68,\\
\alpha_k &= 1,\\
\alpha_\epsilon &= 1.3.
\end{aligned} \tag{6}$$

The source term $R_\varepsilon$ in the $\varepsilon$-equation is

$$\begin{aligned}
R_\varepsilon &= \frac{\rho C_\mu \eta^3}{1+\beta\eta^3} \frac{\varepsilon^2}{k}\left(1 - \frac{\eta}{\eta_0}\right),\\
\eta_0 &= 4.38,\\
\beta &= 0.012,\\
\eta &= \frac{\text{sk}}{\varepsilon}.
\end{aligned} \tag{7}$$

The turbulent thermal conductivity $(k_t)$ is defined as

$$k_t = c_p \frac{\rho \nu_t}{\text{Pr}_t}. \tag{8}$$

$\text{Pr}_t$ is the turbulent Prandtl number (0.71535).

As mentioned before, the dispersion pattern of the exhaled air is traced by tracer gas $N_2O$. The conservation equation in the species transport model is

$$\frac{\partial}{\partial t}(\rho Y_i) + \nabla \cdot \left(\rho \vec{V} Y_i\right) = \nabla\left[\left(\rho D_{i,m} + \frac{\mu_t}{Sc_t}\right)\nabla Y_i\right], \tag{9}$$

where $D_{i,m}$ is the mass diffusion coefficient for species in the mixture, and the turbulent Schmidt number $Sc_t = \mu_t/\rho D_t$ is set to 0.7.

The wall enhancement model has been applied to capture the viscous sublayer because of the high-resolution grid near the wall (human body), which results in a maximum value of $Y^+$ of about 5.5.

*3.2. Computational Grid and Validation.* In the current simulation, the computational grid was divided into blocks, with a higher density near human bodies than at the cabin's center. The breathing zone was refined to capture the interaction of exhalation and thermal plume, as seen in Figure 5. The cell number in the computational domain before the adaption was 5.5 million, which increased to 17 million cells after the adaption. The cell number was selected 5.5 million based on the grid study (the grid convergence index (GCI) for the 5.5 and 7.7 million nods is 4.8% and 2.1%) as illustrated in Figure 6. As seen, a negligible deviation was observed in velocity profile 6 cm above the human head (see line 1 in Figure 2) when the cell number exceeds 5.7 million. Hence, this intermediate grid size was used for the simulation which the maximum value of the $Y^+$ and skewness is 0.5 and 0.8, respectively.

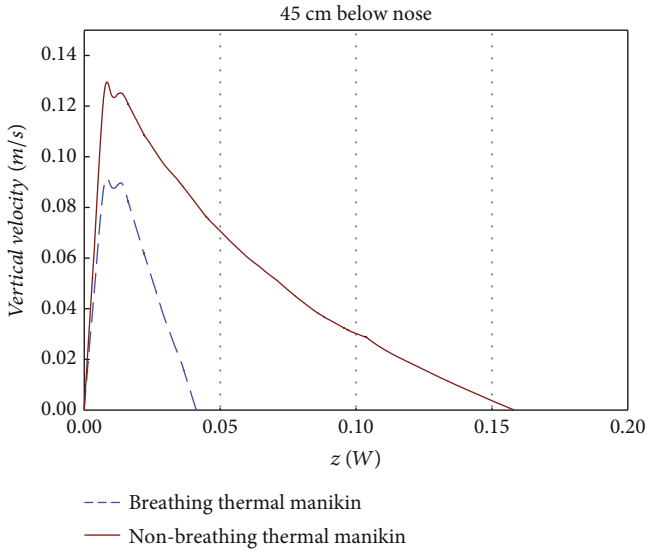


Figure 9: Velocity profile of the human thermal plume with and without breathing.

The maximum velocity of the human thermal plume is affected by the temperature difference between the human body surface and the environment, thermal manikin geometry, clothing, and the human's leaning, sitting, or standing position. Based on the literature, the maximum velocity of the thermal plume ranges between 0.2 and 0.35 m/s [70]. Due to different geometrical characteristics of the human body and boundary conditions, an exact quantitative comparison with other experiment data was difficult. However, in Table 4, the maximum velocity of the thermal plume (6 cm above the human's head, see line 1 in Figure 2) is compared with the previous numerical and experimental results. Based on Table 4, the maximum velocity in the current simulation has a good consistency with the literature.

## 4. Results

In the current investigation, the elevator's cabin flow field, heat transfer, and species transport are simulated for 4 breathing cycles (i.e., over 24 seconds). The elevator moves up from the ground floor to the 24th floor nonstop. Six thermal manikins are in the elevator and are breathing through their noses.

To better understand how the human thermal plume interacts with breathing, we perform two additional simulations, one without the thermal effects (case 2: isothermal breathing manikin), and one without breathing (case 3:

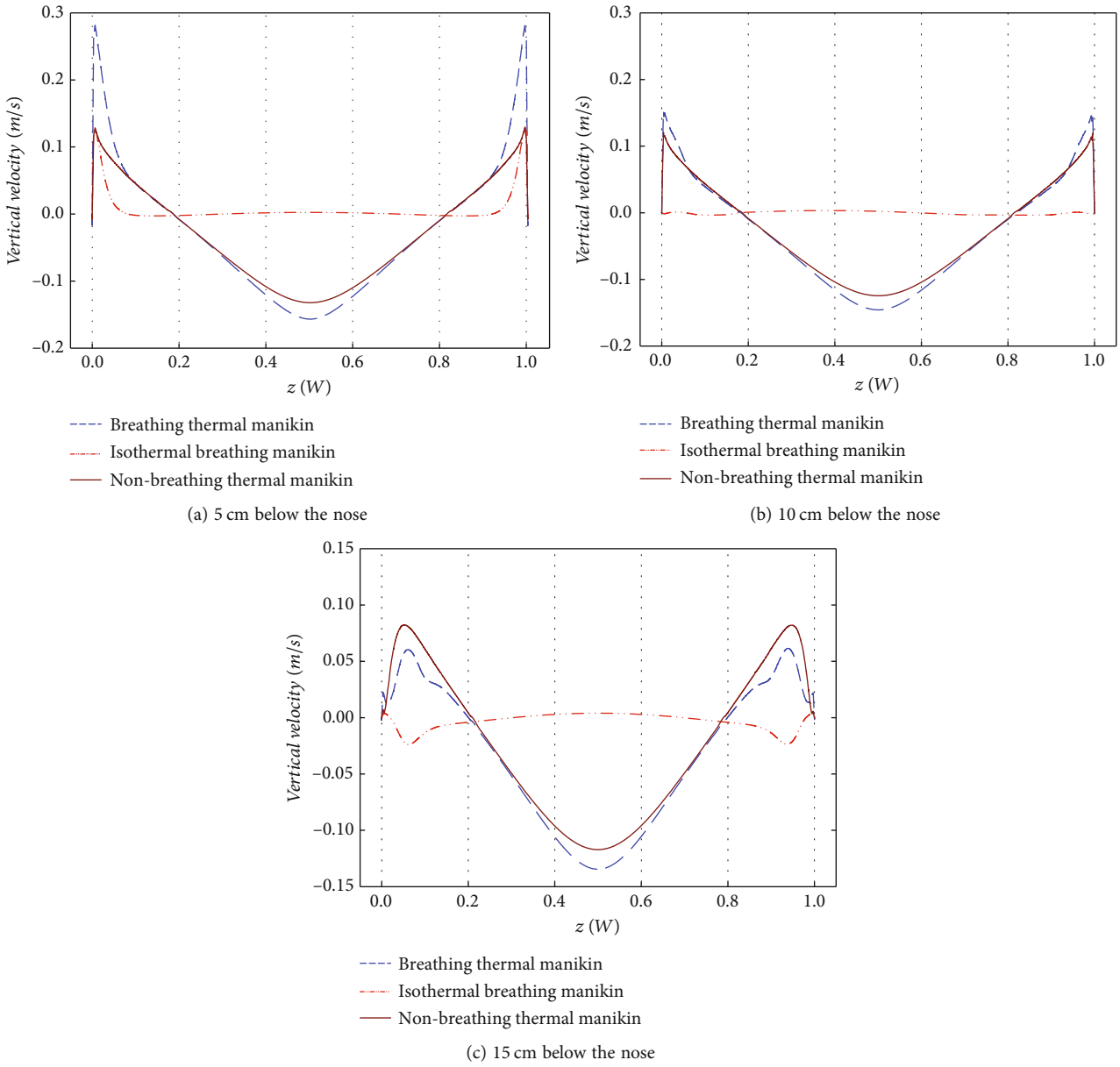


Figure 10: Velocity profile in the middle of the cabin at different distances of the nose during inhalation.

nonbreathing thermal manikin). Then, careful intercomparisons between the based case (case 1: breathing thermal manikin) and the two simplified cases are performed to precisely assess the roles that different mechanisms play in determining the resulting flow field. Results include the velocity profile in the center of the elevator cabin, boundary layer characteristics of the human thermal plume, streamlines, and the time-dependent heat transfer rates for the different sections of the human body.

*4.1. Interaction of the Human Thermal Plume with Breathing during Exhalation.* We first consider the exhalation phase. Figure 7 shows the vertical velocity distribution of the nonbreathing thermal manikin at 19.5 seconds (the middle of the fourth exhalation when the downward exhaled air velocity takes the maximum value), along the horizontal line located 10 cm below the nose in the middle of the elevator cabin. In Figure 7, the horizontal axis is along the $Z$-direction (see Figure 2) which is nondimensionalized by the width of the cabin ($W$) ($z/W = 0$ and $Z/w = 1$ indicate the human's location on the left and right side of the elevator cabin). In this case, only the natural convection driven by the temperature difference between the body surface and the indoor environment is present, creating an upward thermal plume flow near the human body surface and the maximum velocity is 0.11 m/s. As mentioned before, many researchers have studied the characteristics of the human thermal plume, but the fate of the plume in a closed environment has not been discussed. As seen in Figure 7, in the center of the elevator's cabin without any ventilation system,

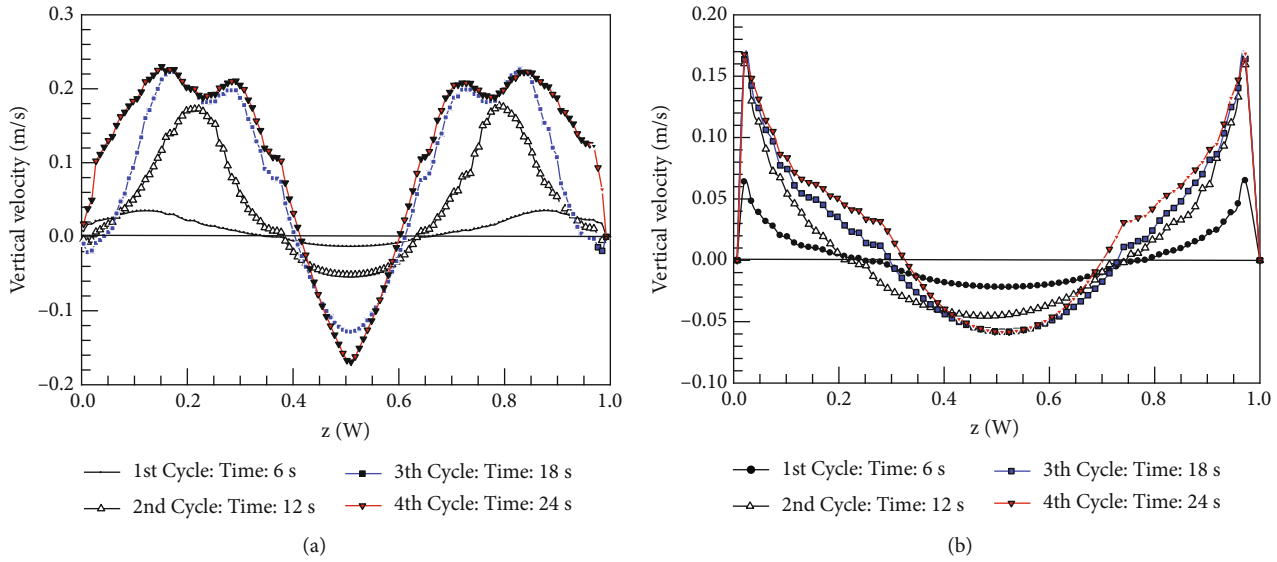


Figure 11: Vertical velocity profile in different times. (a) 10 cm below the head and (b) 90 cm above the head.

there is a downward vertical flow, and the value of the downward velocity of the order 0.1 m/s which the reflection of the thermal plume by the ceiling leads to a circulation flow and the downward velocity that is comparable with the thermal plume velocity.

Figures 8(a), 8(b), and 8(c) illustrate the effect of breathing through the nose on the vertical velocity distribution at distances of 10, 20, and 45 cm below the nose (see Figure 2), respectively. These figures present the decay rate of the exhaled jet, the penetration length of the exhaled jet with and without thermal plume, and the effect of the exhaled jet on the local flow velocity near the human body (i.e., the microenvironment). As seen, in the case of the isothermal breathing manikin, the maximum downward velocity is −2.45, −1.78, and −0.42 m/s at 10, 20, and 45 cm below the nose, respectively; whereas for the case of the breathing thermal manikin, it is −2.42, −1.66, and −0.078 m/s, respectively. It indicates that the upward thermal plume increases the decay rate of the exhaled jet. At 45 cm below the nose, for the case of the breathing thermal manikin the thermal plume overcomes the exhaled jet, and there is an upward velocity of +0.09 m/s in the very vicinity of the human body. The peak maximum followed by a peak minimum near the body for the base case in Figure 9 reflects the competing actions of the body thermal plume and the exhalation jet.

Figure 9 (a zoom-in view of Figure 8(c)) compares the velocity profile near the body surface with and without breathing and shows the effect of the interaction of the human thermal plume and exhalation on the velocity in the thermal boundary layer. As seen, at 45 cm below the nose, in the case of the nonbreathing thermal manikin, the maximum upward velocity of the thermal plume is 0.13 m/s. The thickness of the velocity boundary layer, as measured by the width of positive vertical velocity, is 0.157 m, which is consistent with the literature as the reported value varied 0.1-0.2 m [62, 71]. On the other hand, in the case of the breathing thermal manikin, the maximum upward velocity of the thermal plume is 0.09 m/s, and the thickness of the thermal boundary layer is reduced to 0.04 m by the outside competing downward breathing jet. It can be concluded that the exhalation process disturbs the human thermal plume and decreases its strength. Indeed, exhalation can prevent the entrance of any contaminant, coming from below, into the nasal system, which thermal plume could otherwise carry.

*4.2. Interaction of the Human Thermal Plume with Breathing during Inhalation.* As shown in the previous figures, the downward exhaled jet disturbs the upward boundary layer of the human thermal plume, but the effect of the inhalation is entirely different. It can facilitate the upward movement of the human thermal plume and increases the human thermal plume velocity. Increasing upward velocity can increase the risk of inhaling contaminants such as virus aerosols into the nasal system. Figure 10 shows the velocity variation elevator's cabin center at 5, 10, and 15 cm below the nose. In Figure 10(a), the velocity profiles, 5 cm below the nose in the center of the elevator cabin, at 22.5 seconds (the middle of the fourth inhalation when the upward inhaled velocity takes the maximum value), are illustrated and compared in the three cases. In the case of nonbreathing thermal manikins, the maximum thermal plume's velocity is equal to the maximum velocity of isothermal breathing manikins, which is induced by exhalation and is about 0.12 m/s. In comparison, the maximum velocity near the breathing thermal manikin is 0.29 m/s, more than twice the maximum for the other two cases. In other words, the inhalation process significantly accelerated the human thermal plume in the microenvironment due to the induced upward velocity. Increasing the human thermal plume velocity by inhalation also strengthens the large-scale circulation flow, as observed by the increasing magnitude of the center downward velocity, from 0.13 m/s for the nonbreathing thermal manikins to 0.16 m/s for the thermal breathing manikin. In contrast,

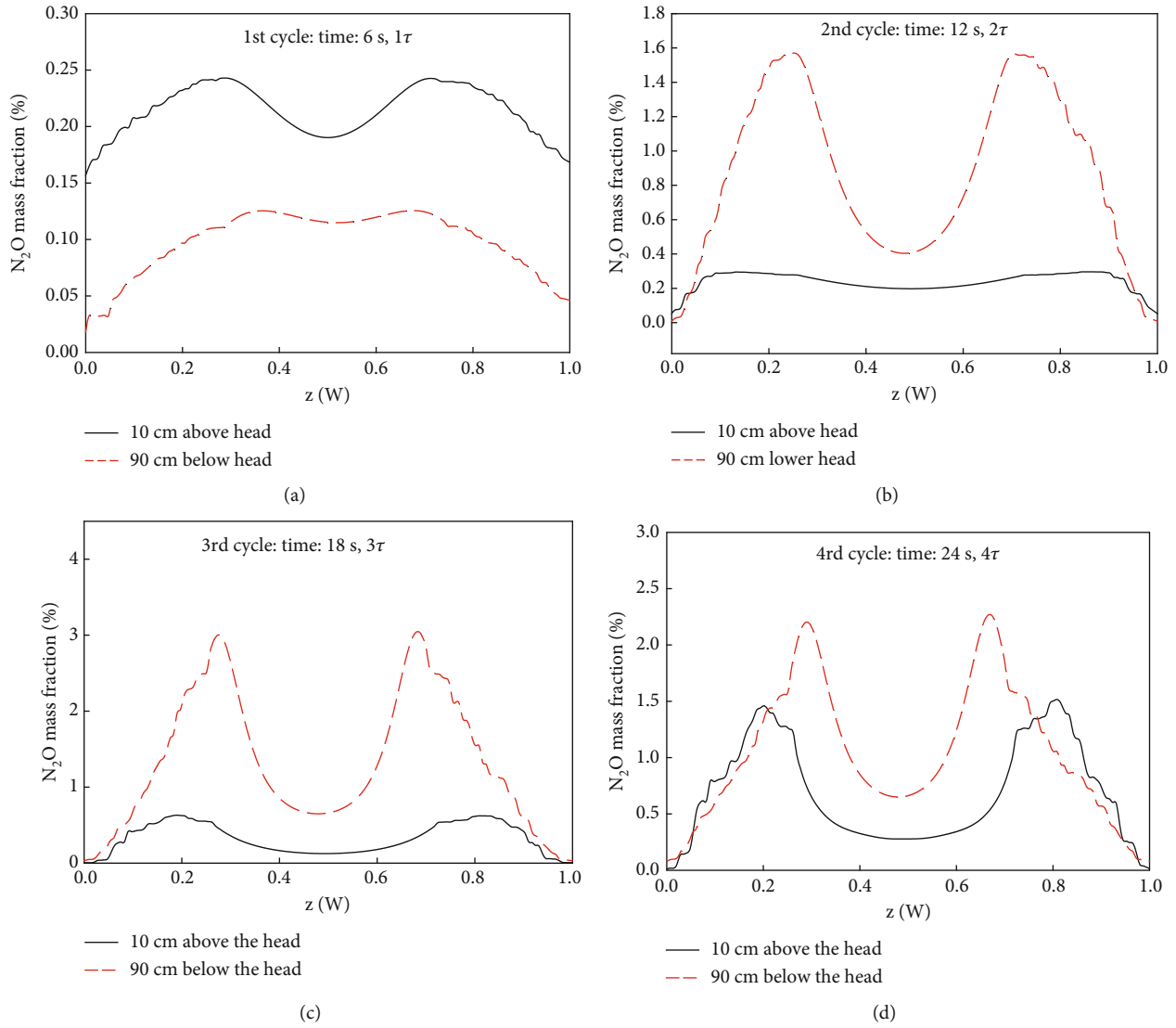


FIGURE 12: $N_2O$ mass fraction below and above the head: (a) the first cycle 6 s, (b) the second cycle 12 s, (c) the third cycle 1 s, and (d) the fourth cycle 24 s.

the inhalation or exhalation alone, as in the case of isothermal breathing manikins shown in Figures 8 and 10, did not generate this large-scale motion in the macroenvironment. This implies that the human thermal plume alone generates more kinetic energy than the breathing jet, as the breathing jet has a larger maximum velocity and is narrowly localized and contains less integral momentum flux, a point to be quantified in Section 4.6.

Figure 10(b) shows the velocity distributions at 10 cm below the nose. It is evident that the inhalation process continues to affect the downward center velocity of the circulation flow. Still its effect on the thermal plume near the body becomes less evident as the distance from the nose is increased.

The velocity distributions at 15 cm below the nose, shown in Figure 10(c), clearly show how the human thermal plume and respiratory activities can affect the microenvironment's characteristics.

In the case of the isothermal breathing manikin, there is a downward velocity in the vicinity of the human body surface, which is induced by the previous exhalation process. This memory effect also explains the slightly reduced upward velocity near the body in the breathing thermal manikin case compared to the nonbreathing thermal manikin. The above results reveal that the inhalation and exhalation jets strongly affect the human thermal plume velocity in the microenvironment.

*4.3. Unsteady Flow Characteristics in the Case of Breathing Thermal Manikins.* Next, we present the exhaled contaminant ($N_2O$) distribution and the velocity profile at the end of the four respiratory cycles (6, 12, 18, and 24 seconds), for the breathing thermal manikins case. Figures 11(a) and 12(b) illustrate the vertical velocity profiles at 10 cm above and 90 cm below the head, respectively. At 10 cm above the head (Figure 11(a)), it takes roughly three full breathing

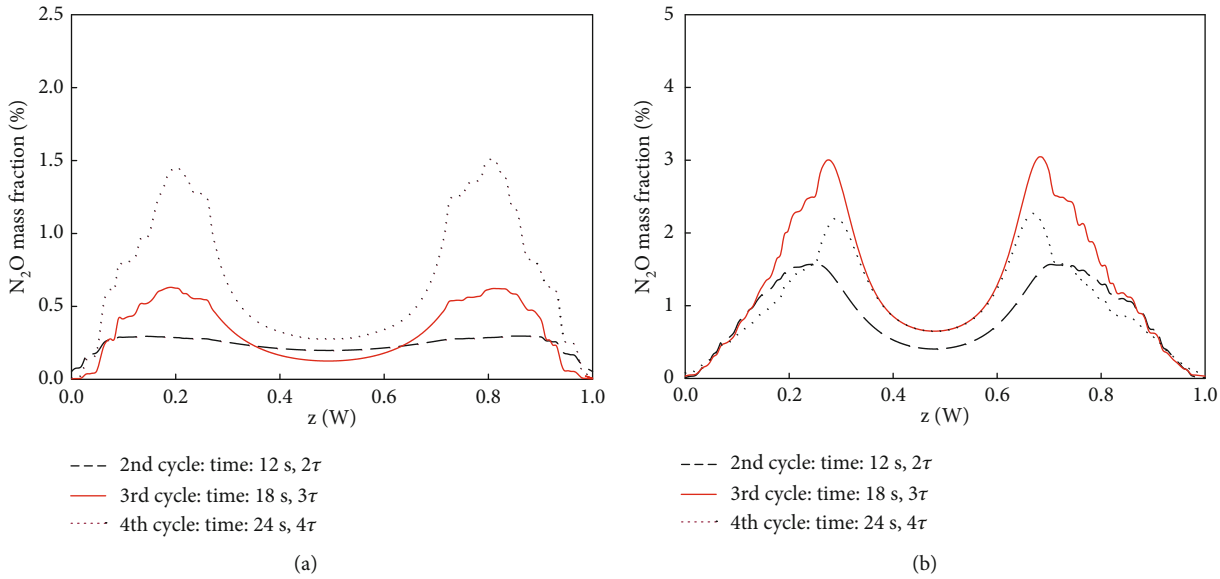


Figure 13: $N_2O$ mass fraction: (a) 10 cm above the head and (b) 90 cm below the head.

cycles for the flow field to develop and reach a maximum upward velocity of about 0.22 m/s. The vertical velocity above the head is positive, and the ceiling reflects this upward flow and generates a vertical downward flow in the center region ($0.4 < Z/W < 0.6$), with a velocity magnitude comparable to the upward velocity of the human thermal plume.

Figure 11(b) displays the velocity profiles 90 cm below the head. The area affected by the thermal plume (where the velocity is positive) changes over time, while the maximum speed in the thermal plume and the magnitude of the downward velocity in the cabin center stabilize after 18 seconds. According to Figure 11(b), at the end of the first respiratory cycle (6 seconds), the maximum velocity of the thermal plume is 0.065 m/s. The width of the human thermal plume is 24 cm, whereas, at the end of the second respiratory cycle (12 seconds), the peak velocity of the thermal plume has increased to 0.18 m/s. The expanding thermal plume at this lower vertical position facilitates upward contaminant transport. The centerline velocity varies, from -0.02 m/s at 6 s to –0.045 m/s at 18 s. The width of the thermal plume is increased to 33 cm at 18 s, while the maximum velocity of the thermal plume does not change much after the second cycle. After the third cycle, the vertical centerline velocity is also saturated, while the width of the thermal plume can further increase (to 39 cm at 24 s). The overall observation here is that the thermal plume intensifies over time, generating a large-scale circulation and a downward flow in the cabin center region.

Figure 12 shows the distribution of contaminants at the same two heights at the end of each breathing cycle. At the end of the first breathing cycle (Figure 13(a)), there is more contamination above the head than below, due to the upward flow in the human thermal plumes, which develops relatively quickly, and the fact that the center downward velocity has not yet fully developed (see Figure 12). At the end of the second breathing cycle (Figure 12(b)), the contaminant level at 90 cm below the head significantly increases; and at the end of the third cycle (Figure 12(c)), the mass fraction below the head reaches its maximum level. During the fourth cycle, the contaminant level at 90 cm below decreases and that at 10 cm above catches up; in other words, the contaminant becomes better mixed in the cabin (Figure 12(d)).

The $N_2O$ dispersion below and above the head at different times are compared in Figures 13(a) and 13(b). As shown, the amount of the contaminant above the head increases gradually over time because of the rising thermal plume, whereas the contaminant dispersion at 90 cm below the head has a more nonmonotonic time dependence, with the maximum contaminant level at the end of the third breathing cycle (18 seconds). These will be further explained by the time evolution of the flow pattern and vortex strength in the lower and upper heights, to be discussed next.

*4.4. Time Evolution of the Multiscale Flow Pattern.* This section examines the streamlines and distribution of the velocity and $N_2O$ mass fraction at different times for the breathing thermal manikin case. Figure 14 shows the streamlines overlayed with the contours of the vertical velocity during four breathing cycles. The streamlines during the first breathing cycle, including the middle of the first exhalation (1.5 seconds), the middle of the first inhalation (4.5 seconds), and at the end of the inhalation (6 seconds), are depicted in Figures 14(a), 14(b), and 14(c), respectively. As seen in Figure 14(a), during the first exhalation, there is a ring vortex caused by the exhaled jet, and the exhaled air penetrates downward and inhibits the rising of the human thermal plume. The area where the vertical velocity is negative (downward flow) is colored in Figure 14(a). At the earlier time (1.5 seconds), the flow around the head is divided into two parts. The first part is the thermal plume that rises between the body and the cabin's wall, and after bypassing the human head, it is reflected by the ceiling and returns

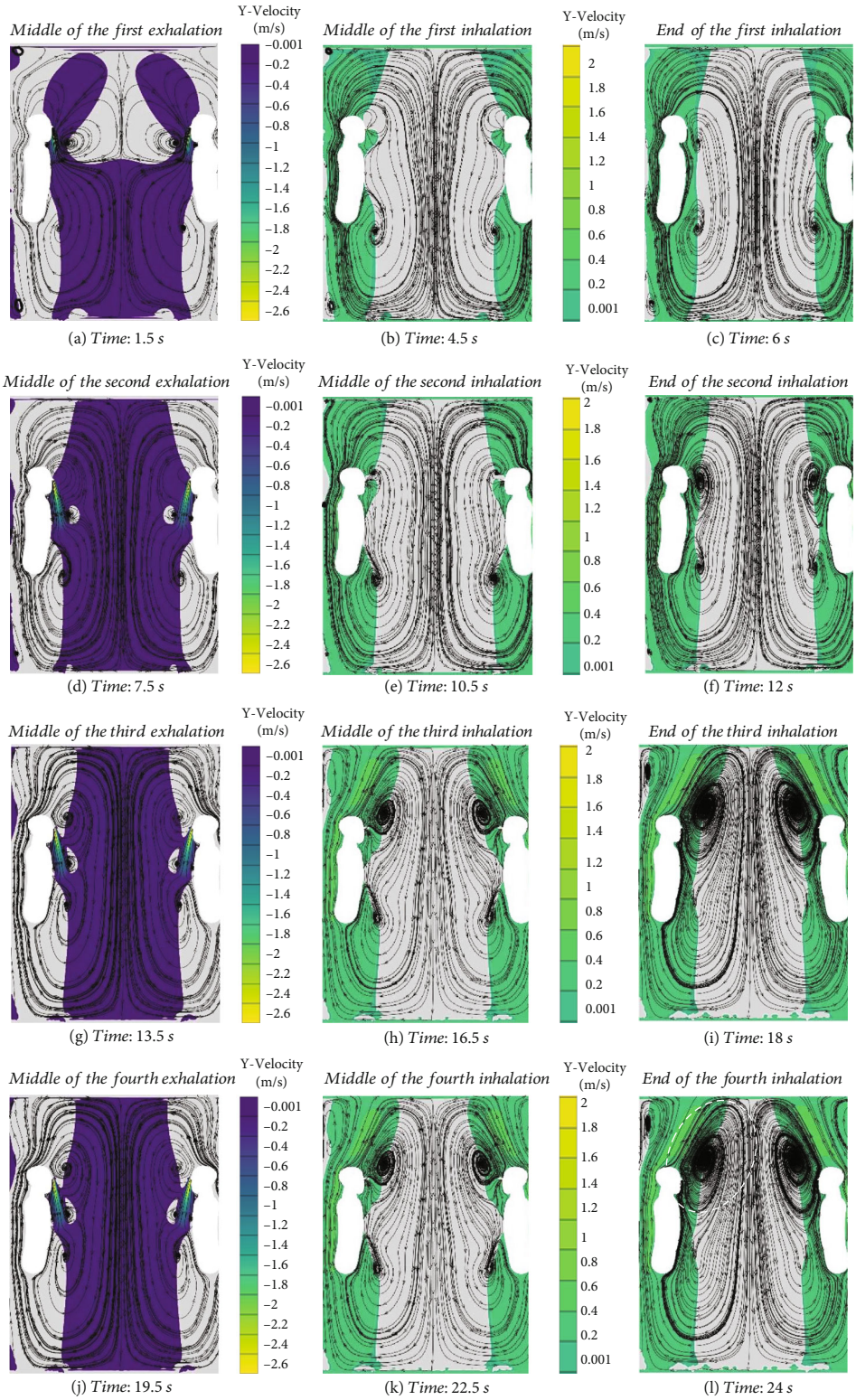


Figure 14: Streamlines and velocity distribution in different times.

to the elevator center, creating a vertical downward flow. The second part is affected by the ring vortex which joins the breathing zone. The flow patterns in Figures 14(b) and 14(c) show the thermal plume rising and being reflected by the cabin's ceiling, creating two separated zones on the left and right sides. The flow pattern on each side reveals that three zones are in front of the human during the first inhalation (Figure 14(b)), including (a) the breathing zone, which penetrates the nasal system; (b) the downward flow caused by the previous exhalation; and (c) the vortex

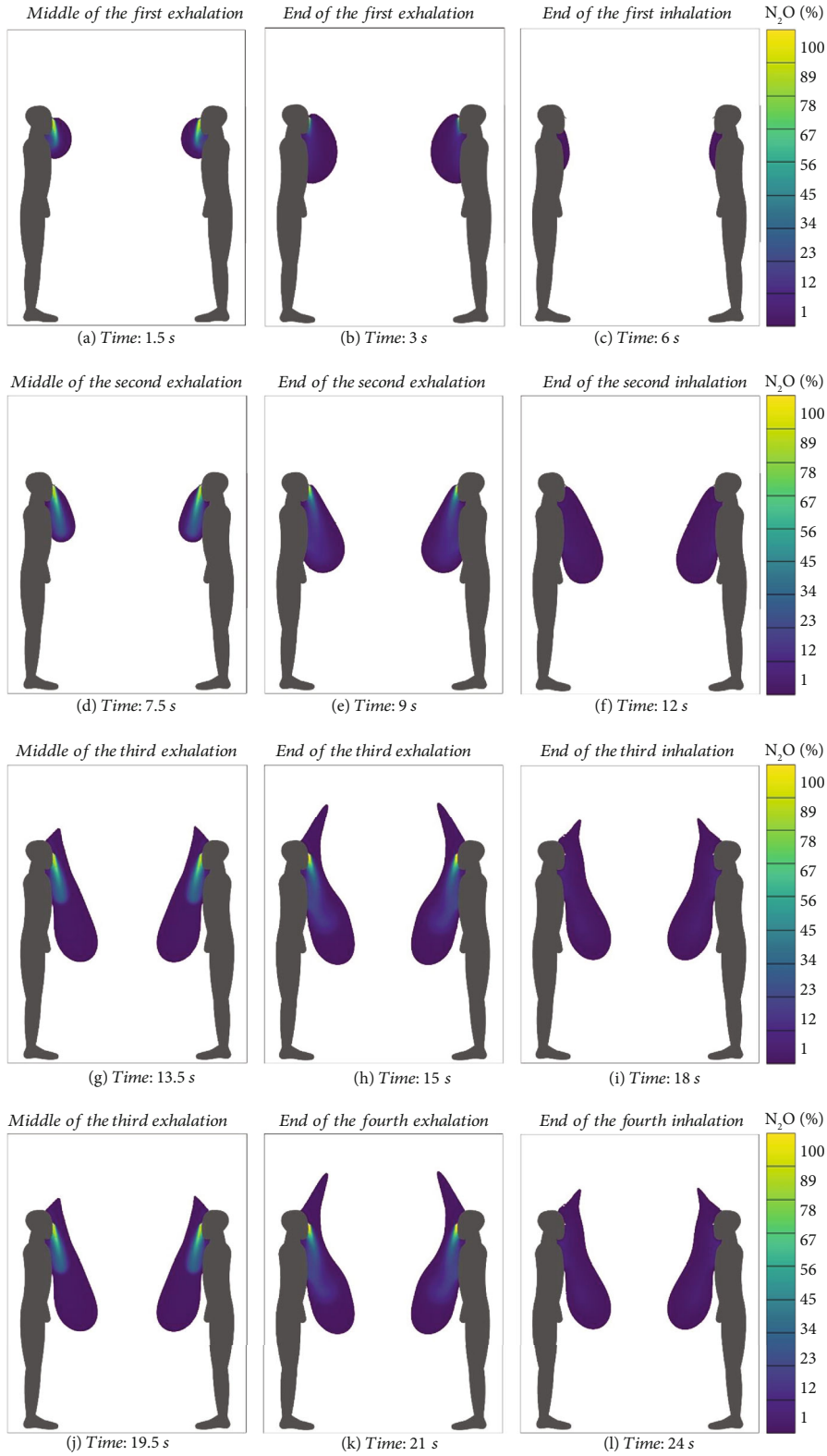


Figure 15: $N_2O$ mass fraction distribution in different times.

generated by the upward thermal plume interacting with the downward circulated flow. Based on Figure 14(c), the inhalation process now eliminates the downward flow due to the previous exhalation. Although exhalation delays upward contaminant penetration until the middle of inhalation (Figure 14(b)), the thermal plume eventually overcomes this downward flow during the second half of inhalation, and it can now carry contaminants upward.

Table 5: Comparison of the heat transfer coefficients of thermal manikin with the literature.

| References | Method | Heat transfer coefficient ($W/m^2$-K) |
|---|---|---|
| Flat vertical plate | Empirical correlations | 2.89 |
| Murakami et al. [72] | CFD | 4.3 |
| Brohus [73] | Experiment | 3.86 |
| de Dear et al. [74] | Experiment | 3.4 |
| Current result | Thermal breathing manikin | 4.4 |
| | Nonbreathing thermal manikin | 3.12 |

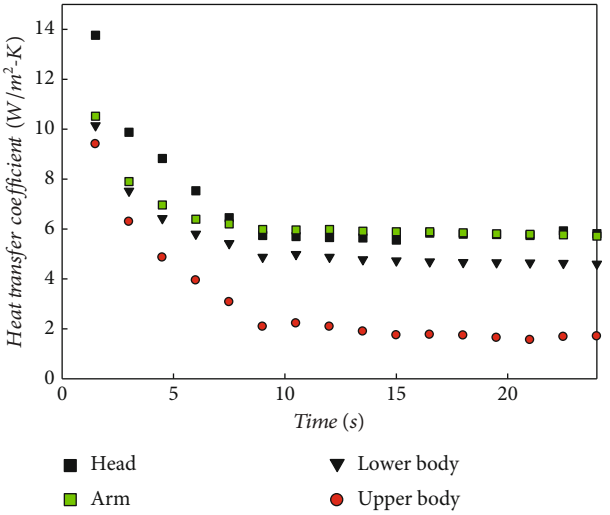


Figure 16: Convective heat transfer coefficients for different segments of a seated human body in the elevator cabin.

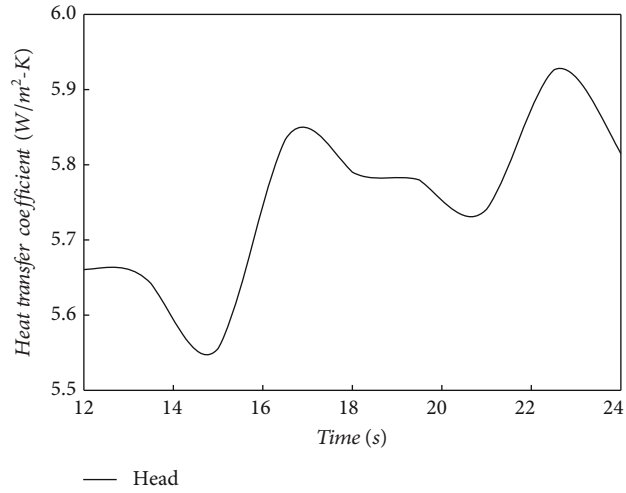


Figure 17: Effect of the exhalation and inhalation on the convective heat transfer coefficient of the head.

The vortex ring generated by inhalation and exhalation can contribute significantly to transferring of contaminants to the nasal area. During exhalation, a counterclockwise vortex ring transports contaminants away from the microenvironment, whereas a clockwise vortex ring moves contaminants into the microenvironment during inhalation.

In other breathing cycles (Figures 14(d), 14(e), 14(f), 14(g), 14(h), 14(i), 14(j), 14(k), and 14(l)), the vertically downward flow in the middle of the elevator is more stable, while the created vortices above and below the head show different behaviors. Based on Figure 14(l), the dashed line indicates that the vortex above the head became stronger at the end of the fourth breathing cycle, causing contaminants to accumulate above the head (as shown and discussed in Figure 13).

According to the current findings, the flow field is divided into two parts on the left and right hand. There are distinct zones on each side, split by the downward vertical flow in the cabin's center. If, however, the macroenvironment flow field is altered, for example, by a ceiling air circulator, the left side and right side can mix, increasing the risk of contaminant dispersion between the two sides. Therefore, in designing an elevator ventilation system, avoiding equipment that causes internal mixing or increases the turbulent intensity is advised.

Figure 15 shows the time evolution of nondimensional $N_2O$ distribution. As mentioned before, the flow pattern, including the downward flow in the center of the cabin, and the shapes of the vortices formed during the inhalation and exhalation process change over time. In this regard, the distribution of $N_2O$ is expected to change over time as the flow field changes. Based on Figures 15(a), 15(d), 15(g), and 15(j), respiratory pollutants are dispersed into the environment during exhalation. Over time, the pollutants released by exhalation have an axial and radial distribution. They penetrated to the lower height by exhaled jet and dispersed in the radial direction by the ring vortices. Gradually, with increasing the vortex strength above the human head, the pollutant concentration above the human head increases (Figure 15(k)). According to the results, the pollutant concentration in the center of the elevator is minimal (the nondimensional $N_2O$ is less than 1%) meaning that in reality, the possibility of pollutant transmission seems very unlikely between the person on the right and left side of the cabin as they breathing. It should be noted that although the present study considered conditions in which people breathe inside the elevator car and do not consider possible sneezing and coughing, the present results can be generalized because people usually cover their coughs and sneezes by hand, which can help prevent the spread of the released particles/virus.

*4.5. Heat Transfer in the Microenvironment.* This section investigates the heat transfer from various human body parts over time and compares it with the literature. The convection heat transfer coefficient depends on the boundary layer characteristics and is affected by geometry and environmental conditions. Based on the data in Gao and Niu's [12] review paper, the convection heat transfer coefficient of a

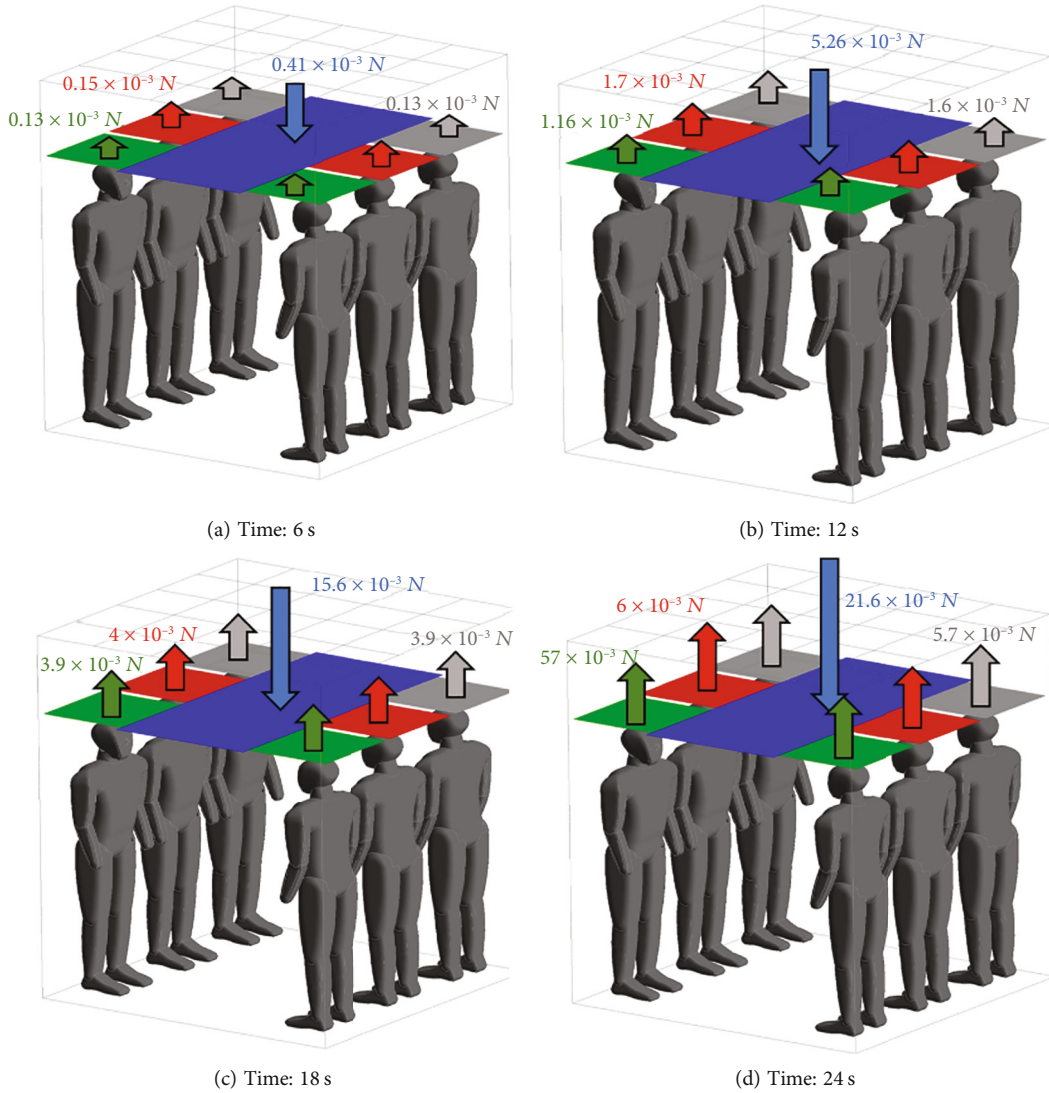


(a) Time: 6 s (b) Time: 12 s

(c) Time: 18 s (d) Time: 24 s

Figure 18: Momentum flux variation above the human head (10 cm).

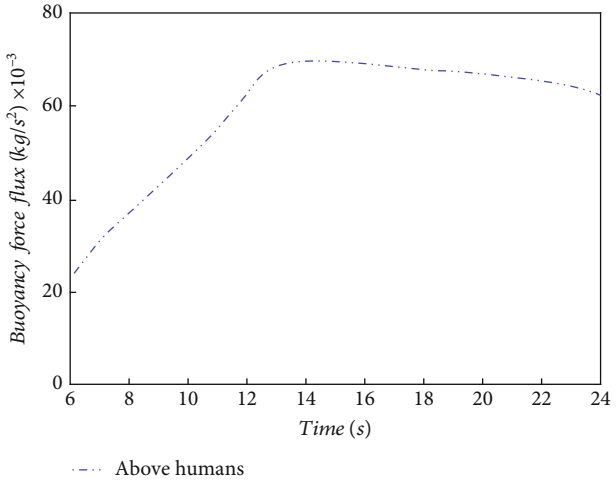


Figure 19: Buoyancy force density variation above the human (10 cm).

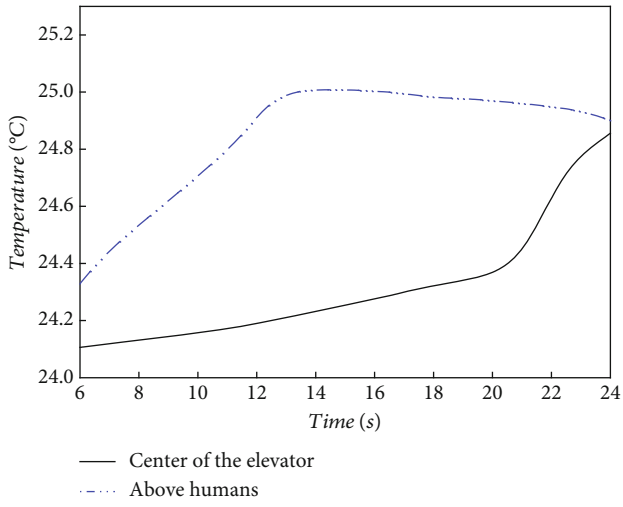


Figure 20: Variation of average temperature above the human (10 cm).

Table 6: Integral characteristics of the thermal plume in the literature and current simulation.

| | Mean velocity (m/s) | Mean volume flux ($m^3/h$) | Mean momentum flux ($N$) | Mean enthalpy flux ($W$) | Mean buoyancy force density ($kg/s^2$) |
|---|---|---|---|---|---|
| Zukowska et al. [75] | — | 258 | 0.008 | 16 | 0.038 |
| Bogdan et al. [6] | 0.0769 | 197 | 0.006 | 27 | 0.013 |
| Zukowska et al. [76] | — | 250 | 0.01 | 26 | 0.006 |
| Current results | 0.075 | 144 | 0.0028 | 26 | 0.008 |

standing human body in the quiescent air varies between 3.9 and 4.3 W/m$^2$-K, as seen in Table 5. The average convective heat transfer coefficients over the body surface and time are computed from our simulations and are presented in Table 5, which shows that our values are similar to previously reported values, indicating that the overall accuracy of our simulations seems to be acceptable.

A literature review shows that the heat transfer coefficient of the human body has been extensively studied. In contrast, data on the variation of heat transfer in each part of the human body as a function of time and especially the effect of respiratory activities such as inhalation and exhalation on the heat transfer rate are rare. Figure 16 shows the variation of the human head, upper body, lower body, and arms' heat transfer coefficient as a function of time. The results show that the heat transfer coefficients from all human body segments decrease in time and then level off. As seen, the heat transfer rate of the upper body is less than the other segments because of the developed boundary layer. The head has the highest heat transfer coefficient, which can be attributed to three factors. First, a higher temperature difference between the head and the environment causes more buoyancy force and increases the local flow velocity. The second is the inhalation and exhalation processes that disturb the boundary layer and increase its local momentum and turbulent intensity. Finally, the third reason may be caused by the chin, which affects the boundary layer arrangement and enhances heat transfer.

Figure 17 presents the effect of breathing on the variation of the convective heat transfer. According to the results, in the exhalation process, the downward exhaled jet reduces the thermal plume's upward velocity, leading to reduced heat transfer. On the other hand, due to the upward induced velocity, the inhalation process accelerates the human thermal plume, thus increasing the heat transfer rate.

*4.6. Analysis of Integral Measures of the Thermal Plume.* Finally, we discuss a few integral parameters of the thermal plume in the elevator. Four integral characteristics are considered: volume flux (kg/m$^3$), momentum flux ($N$), enthalpy flux ($W$), and buoyancy force flux (kg/s$^2$) which are defined by the integration over a given horizontal surface according to [75].

$$\begin{aligned}
\text{Volume flux } \left(\text{kg/m}^3\right) \quad & V = \sum v_y \Delta s, \\
\text{Momentum flux } (N) \quad & I = \sum \rho v_y{}^2 \Delta s, \\
\text{Enthalpy flux } (W) \quad & Q = c_p \sum \rho v_y \Delta T \Delta s, \\
\text{Bsuoyancy force flux } \left(\text{kg/s}^2\right) \quad & P = g\beta \sum \rho \Delta T \Delta s,
\end{aligned} \tag{10}$$

where $V, I, Q$, and $P$ are the volume flux $(m^3/h)$, the momentum flux $(N)$, and the buoyancy force density $(kg/s^2)$, and $Q$ is the enthalpy flux $(W)$, respectively. $v_y$ is the vertical air velocity component (m/s), $\Delta T$ is the air temperature excess (°C), $\Delta s$ is the area of the plume cross-section $(m^2)$, $\rho$ is the air density $(kg/m^3)$, g is the acceleration due to gravity $(m/s^2)$, $\beta$ is the thermal expansion coefficient $(1/K)$, and $C_p$ is the specific heat of air $(j/kg.K)$.These integral measures present characteristics of the driven flow field and heat transfer and the buoyancy force density due to the thermal plume. Examining these integral quantities above the human in the elevator makes it possible to estimate the strength of the upward thermal plume and the reflected downward flow from the ceiling.

Figure 18 presents the momentum flux over several cross sections above the breathing thermal manikins and the central area of the elevator at the end of each respiratory cycle. Figure 18 shows that the momentum flux of the middle manikin is greater than other manikins. The key point in this figure is that the momentum flux of the central cross-section of the elevator is considerable and shows a predominant downward vertical flux in the center of the cabin. The natural downward vertical flow in the center of the cabin caused by the reflection of the human thermal plume should be considered in the ventilation system design for a small closed indoor environment such as an elevator cabin.

In Figures 19 and 20, the variation of the buoyancy force and temperature in terms of time, are illustrated. As seen, in the early time, the boundary layer is forming and rising, which leads to more buoyancy force. Then, it becomes a developed boundary layer, and after 12 seconds, the buoyancy decreases gradually. Bases on Figure 20, the leading cause of increasing temperature in the central cross-section of the elevator is the created ring vortex during exhalation and inhalation that facilitates heat diffusion from the microenvironment to the macroenvironment.

Table 6 compares the integral characteristics of the human thermal plume in the current simulation with those in the literature. Even though the environmental conditions and geometry of the human manikins differ in each study, the integral characteristics are similar. In the studies of Zukowska et al. [75] and Bogdan et al. [6], the manikins were located in the middle of the indoor environment, and the interaction of other humans and the reflecting flow from the ceiling had not been considered. According to the current findings in a close environment, the reflected thermal plume has a significant momentum and enthalpy flux and should be considered in ventilation systems.

## 5. Conclusions

By solving the unsteady RANS equations, the present study performed simulations of the flow field, species transport, and heat transfer in the elevator cabin with six thermal manikins. The breathing cycles and human thermal plume were explicitly modeled, and the exhaled contaminant was considered as a tracer gas ($N_2O$). Three cases, i.e., "breathing thermal plume, isothermal breathing, and nonbreathing thermal manikins" were simultaneously simulated and intercompared. Results showed that the thermal plume and the breathing process contribute to the accurately predicting the multiscale flow field in a closed indoor environment. Based on the results, we found that the human thermal plume affects the microenvironment (thermal boundary layer) and the macroenvironment (cabin-scale flow circulation), and the inhalation process could accelerate the thermal plume and increase the circulation flow's downward velocity. The most important findings from this study are summarized below:

(1) In the case of the "nonbreathing thermal manikin," the human thermal plume caused a circulation in the cabin, and the maximum upward velocity in the vicinity of the body surface was 0.15 m/s, and the velocity of the reflected circulation flow in the center of the cabin was 0.13 m/s

(2) In the case of the "breathing thermal manikin," 5 cm below the nose, during inhalation, the upward velocity of the human thermal plume was 0.29 m/s, whereas it was 0.12 m/s in the case of the "nonbreathing thermal manikin"

(3) In the case of the "breathing thermal manikin," 10 cm below the nose, during exhalation, the velocity of the human thermal plume was −2.5 m/s, whereas it was 0.1 m/s in the case of the "nonbreathing thermal manikin"

(4) The penetration length of the exhaled jet in the case of the "breathing thermal manikin" was about 25 cm, whereas in the case of "isothermal breathing manikin," it could penetrate 45 cm below the nose

(5) In the case of "nonbreathing thermal manikins," at 45 cm below the nose, the boundary layer thickness of the human thermal plume was 16 cm, whereas in the case of the "breathing thermal manikin," it was about 4 cm

(6) Over time, exhalation and inhalation affected the contaminant dispersion by generating local vortices and large-scale circulation flow. At early times, there were two vortices. One was caused by exhalation (ring vortex) near the breathing zone, and the other was caused by the interaction between upward thermal plumes and downward exhaled jets. Over the time, the vortex above the head was the predominant vortex that increased contaminant concentration above the head as the circulation flow in the elevator became more assertive

(7) The heat transfer coefficient of the body surface was affected by inhalation and exhalation processes. The thermal plume accelerated during inhalation, whereas the thermal plume velocity decreased during exhalation. This resulted in increased convection heat transfer during inhalation and decreased convection heat transfer during exhalation

(8) To decrease contaminants dispersion in a closed environment such as the elevator cabin, using any type of ventilation system, such as "a ceiling air circulator," which can create a circular flow pattern and mix left and right side flow, should be avoided. This is because the reflected human thermal plume by the ceiling can separate the left and right sides

Overall, this study evidences that the human thermal plume and breathing activities must be considered to correctly predict the flow field and contaminant dispersion pattern in a closed indoor environment such as an elevator cabin. The authors hope that the current investigation will help in designing new standards for a health-based ventilation system for the elevator cabin to minimize and control the dispersion of contaminants, such as virus aerosols.

## Data Availability

The datasets used and/or analyzed during the current study are available from the corresponding author on reasonable request.

## Conflicts of Interest

The authors declare that they have no conflicts of interest.

## Acknowledgments

This work has been supported by the Science, Technology and Innovation Committee of Shenzhen Municipality (Grant No. 2020-148), the National Natural Science Foundation of China (Grant No. 12041601), the NSFC Basic Science Center Program (Grant No. 11988102), the Taizhou-Shenzhen Innovation Center, Guangdong Provincial Key Laboratory of Turbulence Research and Applications (2019B21203001), and the Guangdong-Hong Kong-Macao Joint Laboratory for Data-Driven Fluid Mechanics and Engineering Applications (2020B1212030001). Computing resources are provided by the Center for Computational Science and Engineering of Southern University of Science and Technology.

## References

[1] E. Ding, D. Zhang, and P. M. Bluyssen, "Ventilation regimes of school classrooms against airborne transmission of infectious respiratory droplets: A review," *Building and Environment*, vol. 207, article 108484, 2022.

[2] Y. Zhou, Y. Deng, P. Wu, and S. J. Cao, "The effects of ventilation and floor heating systems on the dispersion and

deposition of fine particles in an enclosed environment," *Building and Environment*, vol. 125, pp. 192–205, 2017.

[3] T. Zhang, Y. Zhang, A. Li, Y. Gao, Y. Rao, and Q. Zhao, "Study on the kinetic characteristics of indoor air pollutants removal by ventilation," *Building and Environment*, vol. 207, article 108535, 2022.

[4] E. Bjørn and P. V. Nielsen, "Dispersal of exhaled air and personal exposure in displacement ventilated rooms," *Indoor Air*, vol. 12, no. 3, pp. 147–164, 2002.

[5] H. E. Lewis, A. R. Foster, B. J. Mullan, R. N. Cox, and R. P. Clark, "Aerodynamics of the human microenvironment," *The Lancet*, vol. 293, no. 7609, pp. 1273–1277, 1969.

[6] A. Bogdan, K. Ogłodziński, and M. Szyłak-Szydłowski, "Analysis of thermal plumes forming over male human subjects," *Journal of Building Engineering*, vol. 45, article 103596, 2022.

[7] J. Li, J. Liu, C. Wang, N. Jiang, and X. Cao, "PIV methods for quantifying human thermal plumes in a cabin environment without ventilation," *Journal of Visualization*, vol. 20, no. 3, pp. 535–548, 2017.

[8] A. W. Gena, C. Voelker, and G. S. Settles, "Qualitative and quantitative schlieren optical measurement of the human thermal plume," *Indoor Air*, vol. 30, no. 4, pp. 757–766, 2020.

[9] B. A. Craven and G. S. Settles, "A computational and experimental investigation of the human thermal plume," *Journal of Fluids Engineering*, vol. 128, no. 6, pp. 1251–1258, 2006.

[10] Z. Liu, D. Yin, Y. Niu, G. Cao, H. Liu, and L. Wang, "Effect of human thermal plume and ventilation interaction on bacteria-carrying particles diffusion in operating room microenvironment," *Energy and Buildings*, vol. 254, article 111573, 2022.

[11] M. Salmanzadeh, G. Zahedi, G. Ahmadi, D. R. Marr, and M. Glauser, "Computational modeling of effects of thermal plume adjacent to the body on the indoor airflow and particle transport," *Journal of Aerosol Science*, vol. 53, pp. 29–39, 2012.

[12] N. P. Gao and J. L. Niu, "CFD study of the thermal environment around a human body: a review," *Indoor and Built Environment*, vol. 14, no. 1, pp. 5–16, 2005.

[13] G. Feng, Y. Bi, Y. Zhang, Y. Cai, and K. Huang, "Study on the motion law of aerosols produced by human respiration under the action of thermal plume of different intensities," *Sustainable Cities and Society*, vol. 54, article 101935, 2020.

[14] Y. Yan, X. Li, L. Yang, and J. Tu, "Evaluation of manikin simplification methods for CFD simulations in occupied indoor environments," *Energy and Buildings*, vol. 127, pp. 611–626, 2016.

[15] J. Zong, J. Liu, Z. Ai, and M. K. Kim, "A review of human thermal plume and its influence on the inhalation exposure to particulate matter," *Indoor and Built Environment*, vol. 31, no. 7, pp. 1758–1774, 2022.

[16] B. Koelblen and A. Bogdan, "Impact of clothing, breathing and body posture on the shaping of a thermal plume above a human," *International Journal of Ventilation*, vol. 13, no. 4, pp. 397–410, 2015.

[17] A. Papoutsakis, I. Danaila, F. Luddens, and M. Gavaises, "Droplet nuclei caustic formations in exhaled vortex rings," *Scientific Reports*, vol. 12, no. 1, p. 3892, 2022.

[18] K. Liu, M. Allahyari, J. S. Salinas, N. Zgheib, and S. Balachandar, "Peering inside a cough or sneeze to explain enhanced airborne transmission under dry weather," *Scientific Reports*, vol. 11, no. 1, p. 9826, 2021.

[19] X. Deng and G. Gong, "Effects of indoor air stability on exhaled contaminant flow and thermal plume in the interpersonal breathing microenvironment," *International Journal of Thermal Sciences*, vol. 170, article 107173, 2021.

[20] C. Chen, W. Liu, F. Li et al., "A hybrid model for investigating transient particle transport in enclosed environments," *Building and Environment*, vol. 62, pp. 45–54, 2013.

[21] J. M. Villafruela, I. Olmedo, M. Ruiz de Adana, C. Méndez, and P. V. Nielsen, "CFD analysis of the human exhalation flow using different boundary conditions and ventilation strategies," *Building and Environment*, vol. 62, pp. 191–200, 2013.

[22] Z. Cheng, C. Guangyu, A. Aganovic, and L. Baizhan, "Experimental study of the interaction between thermal plumes and human breathing in an undisturbed indoor environment," *Energy and Buildings*, vol. 207, article 109587, 2020.

[23] R. B. Holmberg, L. Eliasson, K. Folkesson, and O. Strindehag, "Inhalation-zone air quality provided by displacement ventilation," in *Proceedings of Roomvent 90, Session B2-2, Paper no 32*, pp. 1–9, Oslo, Norway, 1990.

[24] T. Dbouk and D. Drikakis, "On coughing and airborne droplet transmission to humans," *Physics of Fluids*, vol. 32, no. 5, article 053310, 2020.

[25] Y. Ji, H. Qian, J. Ye, and X. Zheng, "The impact of ambient humidity on the evaporation and dispersion of exhaled breathing droplets: a numerical investigation," *Journal of Aerosol Science*, vol. 115, pp. 164–172, 2018.

[26] M. Hossain and N. H. Faisal, "Modeling aerosol cloud aerodynamics during human coughing, talking, and breathing actions," *AIP Advances*, vol. 11, no. 4, article 045111, 2021.

[27] S. Bhattacharyya, K. Dey, A. R. Paul, and R. Biswas, "A novel CFD analysis to minimize the spread of COVID-19 virus in hospital isolation room," *Chaos, Solitons and Fractals*, vol. 139, article 110294, 2020.

[28] M. S. Islam, P. Larpruenrudee, A. R. Paul et al., "SARS CoV-2 aerosol: how far it can travel to the lower airways?," *Physics of Fluids*, vol. 33, no. 6, article 061903, 2021.

[29] M. Abuhegazy, K. Talaat, O. Anderoglu, and S. V. Poroseva, "Numerical investigation of aerosol transport in a classroom with relevance to COVID-19," *Physics of Fluids*, vol. 32, no. 10, article 103311, 2020.

[30] S. R. Narayanan and S. Yang, "Airborne transmission of virus-laden aerosols inside a music classroom: effects of portable purifiers and aerosol injection rates," *Physics of Fluids*, vol. 33, no. 3, article 33307, 2021.

[31] Y. Zhao, Y. Feng, and L. Ma, "Numerical evaluation on indoor environment quality during high numbers of occupied passengers in the departure hall of an airport terminal," *Journal of Building Engineering*, vol. 51, article 104276, 2022.

[32] K. Talaat, M. Abuhegazy, O. A. Mahfoze, O. Anderoglu, and S. V. Poroseva, "Simulation of aerosol transmission on a Boeing 737 airplane with intervention measures for COVID-19 mitigation," *Physics of Fluids*, vol. 33, 2021.

[33] X. Yang, C. Ou, H. Yang et al., "Transmission of pathogen-laden expiratory droplets in a coach bus," *Journal of Hazardous Materials*, vol. 397, article 122609, 2020.

[34] C. K. Ho and R. Binns, "Modeling and mitigating airborne pathogen risk factors in school buses," *International Communications in Heat and Mass Transfer*, vol. 129, article 105663, 2021.

[35] M. Visone, M. Lanzetta, M. Lappa, C. Lanzaro, and L. Polizio, "Three-dimensional simulation of clouds of multi-disperse evaporating saliva droplets in a train cabin," *Physics of Fluids*, vol. 33, no. 8, article 083318, 2021.

[36] J. Komperda, A. Peyvan, D. Li et al., "Computer simulation of the SARS-CoV-2 contamination risk in a large dental clinic," *Physics of Fluids*, vol. 33, no. 3, article 033328, 2021.

[37] S. Liu, X. Zhao, S. R. Nichols et al., "Evaluation of airborne particle exposure for riding elevators," *Building and Environment*, vol. 207, article 108543, 2022.

[38] T. Dbouk and D. Drikakis, "On airborne virus transmission in elevators and confined spaces," *Physics of Fluids*, vol. 33, no. 1, article 011905, 2021.

[39] N. Sen, "Transmission and evaporation of cough droplets in an elevator: numerical simulations of some possible scenarios," *Physics of Fluids*, vol. 33, no. 3, article 033311, 2021.

[40] N. N. Peng, K. W. Chow, and C. H. Liu, "Computational study on the transmission of the SARS-CoV-2 virus through aerosol in an elevator cabin: effect of the ventilation system," *Physics of Fluids*, vol. 33, no. 10, article 103325, 2021.

[41] L. Santamaría Bertolín, J. M. Fernández Oro, K. Argüelles Díaz et al., "Optimal position of air purifiers in elevator cabins for the improvement of their ventilation effectiveness," *Journal of Building Engineering*, vol. 63, article 105466, 2023.

[42] R. Biswas, A. Pal, R. Pal, S. Sarkar, and A. Mukhopadhyay, "Risk assessment of COVID infection by respiratory droplets from cough for various ventilation scenarios inside an elevator: an OpenFOAM-based computational fluid dynamics analysis," *Physics of Fluids*, vol. 34, no. 1, article 013318, 2022.

[43] C. Du and Q. Chen, "Virus transport and infection evaluation in a passenger elevator with a COVID-19 patient," *Indoor Air*, vol. 32, no. 10, Article ID e13125, 2022.

[44] M. Kilic and G. Sevilgen, "Modelling airflow, heat transfer and moisture transport around a standing human body by computational fluid dynamics," *International Communications in Heat and Mass Transfer*, vol. 35, no. 9, pp. 1159–1164, 2008.

[45] A. Q. Ahmed, S. Gao, and A. K. Kareem, "Energy saving and indoor thermal comfort evaluation using a novel local exhaust ventilation system for office rooms," *Applied Thermal Engineering*, vol. 110, pp. 821–834, 2017.

[46] P. V. Nielsen, S. Murakami, S. Kato, C. Topp, and J.-H. Yang, *Benchmark Tests for a Computer Simulated Person; Aalborg University: Aalborg, Denmark*, Indoor Environmental Engineering, San Francisco, CA, US, 2003, Available online: https://Www.Cfd-Benchmarks.Com/.

[47] L. F. Grymer, O. Hilberg, O. F. Pedersen, and T. R. Rasmussen, "Acoustic rhinometry: values from adults with subjective normal nasal patency," *Rhinology*, vol. 29, no. 1, pp. 35–47, 1991.

[48] F. Pourfattah, L.-P. Wang, W. Deng, Y.-F. Ma, L. Hu, and B. Yang, "Challenges in simulating and modeling the airborne virus transmission: a state-of-the-art review," *Physics of Fluids*, vol. 33, no. 10, article 101302, 2021.

[49] Y. Zhang, G. Feng, Z. Kang, Y. Bi, and Y. Cai, "Numerical simulation of coughed droplets in conference room," *Procedia Engineering*, vol. 205, pp. 302–308, 2017.

[50] A. Fabregat, F. Gisbert, A. Vernet, S. Dutta, K. Mittal, and J. Pallarès, "Direct numerical simulation of the turbulent flow generated during a violent expiratory event," *Physics of Fluids*, vol. 33, no. 3, article 035122, 2021.

[51] H. Qian, Y. Li, P. V. Nielsen, and C. E. Hyldgaard, "Dispersion of exhalation pollutants in a two-bed hospital ward with a downward ventilation system," *Building and Environment*, vol. 43, no. 3, pp. 344–354, 2008.

[52] J. K. Gupta, C.-H. Lin, and Q. Chen, "Characterizing exhaled airflow from breathing and talking," *Indoor Air*, vol. 20, no. 1, pp. 31–39, 2010.

[53] A. Naseri, O. Abouali, and G. Ahmadi, "Effect of turbulent thermal plume on aspiration efficiency of micro-particles," *Building and Environment*, vol. 118, pp. 159–172, 2017.

[54] E. Bjørn, *Simulation of Human Respiration with Breathing Thermal Manikin*, Dept. of Building Technology and Structural Engineering, Aalborg University, Aalborg, 2000.

[55] J. Hang, Y. Li, and R. Jin, "The influence of human walking on the flow and airborne transmission in a six-bed isolation room: tracer gas simulation," *Building and Environment*, vol. 77, pp. 119–134, 2014.

[56] J. Li, J. Liu, J. Pei, K. Mohanarangam, and W. Yang, "Experimental study of human thermal plumes in a small space via large-scale TR PIV system," *International Journal of Heat and Mass Transfer*, vol. 127, pp. 970–980, 2018.

[57] J. Ma, H. Qian, P. V. Nielsen, L. Liu, Y. Li, and X. Zheng, "What dominates personal exposure? Ambient airflow pattern or local human thermal plume," *Building and Environment*, vol. 196, article 107790, 2021.

[58] W. Abou Hweij, N. Ghaddar, K. Ghali, and C. Habchi, "Optimized performance of displacement ventilation aided with chair fans for comfort and indoor air quality," *Energy and Buildings*, vol. 127, pp. 907–919, 2016.

[59] S. Liying, T. Shuang, and Z. Lujie, "Working parameter selection and analysis of radiant floor cooling combined with desk-based task/ambient conditioning (TAC) system," *Building Services Engineering Research and Technology*, vol. 38, no. 1, pp. 104–120, 2017.

[60] X. Li, K. Inthavong, and J. Tu, "Numerical investigation of micron particle inhalation by standing thermal manikins in horizontal airflows," *Indoor and Built Environment*, vol. 25, no. 2, pp. 357–370, 2016.

[61] Q. Ge, X. Li, K. Inthavong, and J. Tu, "Numerical study of the effects of human body heat on particle transport and inhalation in indoor environment," *Building and Environment*, vol. 59, pp. 1–9, 2013.

[62] Y. Liu, Z. Liu, and J. Luo, "Numerical investigation of the unsteady thermal plume around human body in closed space," *Procedia Engineering*, vol. 121, pp. 1919–1926, 2015.

[63] M. Amiraslanpour, J. Ghazanfarian, H. Nabaei, and M. H. Taleghani, "Evaluation of laminar airflow heating, ventilation, and air conditioning system for particle dispersion control in operating room including staffs: a non-Boussinesq Lagrangian study," *Journal of Building Physics*, vol. 45, no. 2, pp. 236–264, 2021.

[64] J. M. Villafruela, I. Olmedo, and J. F. San José, "Influence of human breathing modes on airborne cross infection risk," *Building and Environment*, vol. 106, pp. 340–351, 2016.

[65] S. Sadrizadeh, A. Tammelin, P. Ekolind, and S. Holmberg, "Influence of staff number and internal constellation on surgical site infection in an operating room," *Particuology*, vol. 13, pp. 42–51, 2014.

[66] R. S. Papineni and F. S. Rosenthal, "The size distribution of droplets in the exhaled breath of healthy human subjects," *Journal of Aerosol Medicine*, vol. 10, no. 2, pp. 105–116, 1997.

[67] L. Morawska, G. R. Johnson, Z. D. Ristovski et al., "Size distribution and sites of origin of droplets expelled from the human respiratory tract during expiratory activities," *Journal of Aerosol Science*, vol. 40, no. 3, pp. 256–269, 2009.

[68] Y. Li, X. Huang, I. T. S. Yu, T. W. Wong, and H. Qian, "Role of air distribution in SARS transmission during the largest nosocomial outbreak in Hong Kong," *Indoor Air*, vol. 15, no. 2, pp. 83–95, 2005.

[69] J. Liu, S. Zhu, M. K. Kim, and J. Srebric, "A review of CFD analysis methods for personalized ventilation (PV) in indoor built environments," *Sustainability*, vol. 11, no. 15, p. 4166, 2019.

[70] C. Xu, P. V. Nielsen, L. Liu, R. L. Jensen, and G. Gong, "Human exhalation characterization with the aid of schlieren imaging technique," *Building and Environment*, vol. 112, pp. 190–199, 2017.

[71] C. Voelker, S. Maempel, and O. Kornadt, "Measuring the human body's microclimate using a thermal manikin," *Indoor Air*, vol. 24, no. 6, pp. 567–579, 2014.

[72] S. Murakami, J. Zeng, and T. Hayashi, "CFD analysis of wind environment around a human body," *Journal of Wind Engineering and Industrial Aerodynamics*, vol. 83, no. 1-3, pp. 393–408, 1999.

[73] H. Brohus, *Personal Exposure to Contaminant Sources in Ventilated Rooms*, Alberg University, 1997.

[74] R. J. de Dear, E. Arens, Z. Hui, and M. Oguro, "Convective and radiative heat transfer coefficients for individual human body segments," *International Journal of Biometeorology*, vol. 40, no. 3, pp. 141–156, 1997.

[75] D. Zukowska, Z. Popiolek, and A. Melikov, "Determination of the integral characteristics of an asymmetrical thermal plume from air speed/velocity and temperature measurements," *Experimental Thermal and Fluid Science*, vol. 34, no. 8, pp. 1205–1216, 2010.

[76] D. Zukowska, A. Melikov, and Z. Popiolek, "Impact of geometry of a sedentary occupant simulator on the generated thermal plume: experimental investigation," *Hvac&R Research*, vol. 18, no. 4, pp. 795–811, 2012.